



**HAL**  
open science

# Deformation behavior of continental crust during subduction and exhumation: Strain distribution over the Tenda massif (Alpine Corsica, France)

Alexandre Beaudoin, Romain Augier, Laurent Jolivet, Anthony Jourdon, Hugues Raimbourg, Stéphane Scaillet, Giovanni Luca Cardello

## ► To cite this version:

Alexandre Beaudoin, Romain Augier, Laurent Jolivet, Anthony Jourdon, Hugues Raimbourg, et al.. Deformation behavior of continental crust during subduction and exhumation: Strain distribution over the Tenda massif (Alpine Corsica, France). *Tectonophysics*, 2017, 705, pp.12-32. 10.1016/j.tecto.2017.03.023 . insu-01502958

**HAL Id: insu-01502958**

**<https://insu.hal.science/insu-01502958>**

Submitted on 8 Apr 2017

**HAL** is a multi-disciplinary open access archive for the deposit and dissemination of scientific research documents, whether they are published or not. The documents may come from teaching and research institutions in France or abroad, or from public or private research centers.

L'archive ouverte pluridisciplinaire **HAL**, est destinée au dépôt et à la diffusion de documents scientifiques de niveau recherche, publiés ou non, émanant des établissements d'enseignement et de recherche français ou étrangers, des laboratoires publics ou privés.

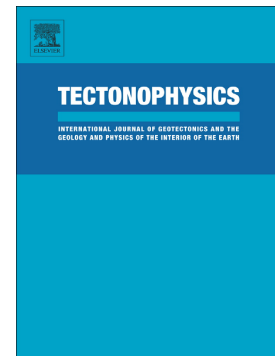


Distributed under a Creative Commons Attribution - NonCommercial - NoDerivatives 4.0 International License

## Accepted Manuscript

Deformation behavior of continental crust during subduction and exhumation: Strain distribution over the Tenda massif (Alpine Corsica, France)

Alexandre Beaudoin, Romain Augier, Laurent Jolivet, Anthony Jourdon, Hugues Raimbourg, Stéphane Scaillet, Giovanni Luca Cardello



PII: S0040-1951(17)30122-1  
DOI: doi: [10.1016/j.tecto.2017.03.023](https://doi.org/10.1016/j.tecto.2017.03.023)  
Reference: TECTO 127440  
To appear in: *Tectonophysics*  
Received date: 4 May 2016  
Revised date: 6 March 2017  
Accepted date: 24 March 2017

Please cite this article as: Alexandre Beaudoin, Romain Augier, Laurent Jolivet, Anthony Jourdon, Hugues Raimbourg, Stéphane Scaillet, Giovanni Luca Cardello , Deformation behavior of continental crust during subduction and exhumation: Strain distribution over the Tenda massif (Alpine Corsica, France). The address for the corresponding author was captured as affiliation for all authors. Please check if appropriate. Tecto(2017), doi: [10.1016/j.tecto.2017.03.023](https://doi.org/10.1016/j.tecto.2017.03.023)

This is a PDF file of an unedited manuscript that has been accepted for publication. As a service to our customers we are providing this early version of the manuscript. The manuscript will undergo copyediting, typesetting, and review of the resulting proof before it is published in its final form. Please note that during the production process errors may be discovered which could affect the content, and all legal disclaimers that apply to the journal pertain.

1 Deformation behavior of continental crust during subduction and exhumation: Strain  
2 distribution over the Tenda massif (Alpine Corsica, France)

3

4 Alexandre Beaudoin<sup>a,b,c,\*</sup>, Romain Augier<sup>a,b,c</sup>, Laurent Jolivet<sup>a,b,c</sup>, Anthony Jourdon<sup>d</sup>, Hugues  
5 Raimbourg<sup>a,b,c</sup>, Stéphane Scaillet<sup>a,b,c</sup>, Giovanni Luca Cardello<sup>e</sup>.

6

7 <sup>a</sup>Université d'Orléans, ISTO, UMR 7327, 45071, Orléans, France

8 <sup>b</sup>CNRS/INSU, ISTO, UMR 7327, 45071, Orléans, France

9 <sup>c</sup>BRGM, ISTO, UMR 7327, 45060, Orléans, France

10 <sup>d</sup>Géoazur, UMR 7329, 06560, Valbonne, France

11 <sup>e</sup>Section des sciences de la Terre et de l'environnement, Université de Genève

12

13 \*Corresponding author: Alexandre Beaudoin, ISTO, 1A rue de la Férollerie, 45071, Orléans,  
14 France (e-mail: [alexandre.beaudoin@univ-orleans.fr](mailto:alexandre.beaudoin@univ-orleans.fr); Tel: +33 2 38 49 25 73)

15

16 Abstract

17

18 In order to address the question of strain localization within continental units during  
19 subduction and exhumation, a large-scale portion of an exhumed continental crust was  
20 structurally revisited. The Tenda massif (Alpine Corsica) has recorded burial (D<sub>1</sub>; top-to-the-  
21 SW kinematics) down to blueschist-facies conditions followed by exhumation (D<sub>2</sub>; top-to-the-  
22 NE kinematics). It was so far regarded as a quite rigid unit with strain localization at the upper  
23 contact with the overlying oceanic material, the East Tenda Shear Zone (ETSZ), where  
24 previous studies were focused. A structural analysis carried out from the core to the  
25 boundaries of this continental unit shows instead that deformation is pervasive in the whole

26 section. A reappraisal of the finite structure shows that this unit corresponds to a N140°E  
27 elongated dome of D<sub>2</sub> fabrics severely overprinting earlier D<sub>1</sub> structures, locally preserved in  
28 the core of the dome. Field observations show that deformation was distributed at maximum  
29 burial, pervasively affecting both the Tenda massif and the overlying tectonically coupled  
30 oceanic material. Strain remained distributed during the first steps of exhumation that  
31 probably started during the last stages of subduction. After a regional switch from  
32 compression to extension, deformation localized toward the ETSZ and other internal shear  
33 zones such as the newly described Saleccia Shear Zone, as shown by strain intensity mapping  
34 in the eastern granitic protoliths. Doming occurred during this localization when crossing the  
35 brittle-ductile transition. This large-scale structural study shows that lithological boundaries  
36 controlled the place where strain localized, while the general style of deformation (distributed  
37 vs localized) was controlled by depth (i.e. pressure-temperature conditions), interacting with  
38 other parameters such as fluid circulation and protolith composition.

39

40 Key-words: Alpine Corsica; Tenda massif; Continental crust; Exhumation; Shear zone; Strain  
41 localization.

42

### 43 1. Introduction

44

45 The progressive deformation of continental basement units from the thrust front to the  
46 internal zones of subduction wedges largely depends upon the rheology of the subducting  
47 lithosphere. In particular, the style of deformation near the thrust front is diagnostic of the  
48 initial rheological stratification of the foreland domain of orogens (Mouthereau et al., 2013).  
49 Although the continental basement is often considered rigid in forelands, the western Alps or  
50 the Zagros show thick-skin deformation near the thrust front where both basement rocks and

51 cover series experienced significant amounts of shortening along localized shear zones active  
52 in the conditions of the greenschist facies (e.g. Leloup et al., 2005; Mouthereau et al., 2007;  
53 Bellahsen et al., 2012; Bellanger et al., 2014). In the internal zones of orogens, continental  
54 units are intensely deformed and sheared in high-pressure and low-temperature (HP-LT)  
55 conditions (blueschists and eclogite facies) during both subduction and exhumation (e.g. Huet  
56 et al., 2009). Thus, from the external to the internal zones, deformation is less and less  
57 localized mainly because temperature increases, but the evolution of continental units  
58 between these two end members is poorly known.

59 The Tenda massif in Alpine Corsica provides an example of subduction of a  
60 continental basement which experienced both intermediate  $P$ - $T$  conditions (lower blueschists  
61 facies) and strong strain localization along the East Tenda Shear Zone (ETSZ), which was  
62 activated during subduction and exhumation (Cohen et al., 1981; Mattauer et al., 1981;  
63 Jourdan, 1988; Jolivet et al., 1990; 1991; Daniel et al., 1996; Molli and Tribuzio, 2004; Molli  
64 et al., 2006; Maggi et al., 2012; 2014; Rossetti et al., 2015).

65 The Alpine Corsica HP-LT orogenic wedge includes both Ligurian oceanic and  
66 European continental units (e.g. Mattauer et al., 1981; Agard and Vitale-Brovarone, 2013;  
67 Vitale-Brovarone et al., 2013). It is part of a larger orogenic system of which the most  
68 external zones are the Provence fold-and-thrust belt and the poorly deformed Western Corsica  
69 Variscan basement (Lacombe and Jolivet, 2005). The internal parts of the wedge, resting on  
70 top of Western Corsica, correspond to a westward-verging stack of nappes characterized by  
71 an eastward metamorphic gradient from lower blueschist-facies in the western continental  
72 Tenda massif to eclogite-facies conditions in the eastern oceanic Schistes Lustrés nappe (e.g.  
73 Mattauer et al., 1981; Lahondère, 1988; Fournier et al., 1991; Caron, 1994; Vitale-Brovarone  
74 et al., 2013). Several tectonometamorphic units are superimposed and separated by tectonic  
75 contacts and sharp metamorphic gaps (Fournier et al., 1991; Caron, 1994; Malavieille et al.,

76 1998; Vitale-Brovarone et al., 2013). The Tenda massif represents a part of the continental  
77 margin involved in the orogenic wedge. It is regarded as a quite rigid block that escaped  
78 significant internal deformation during subduction and exhumation (Mattauer et al., 1981;  
79 Daniel et al., 1996; Gueydan et al., 2003; Molli et al., 2006; Maggi et al., 2012; 2014; Rossetti  
80 et al., 2015) with shearing mostly localized along its eastern margin, the ETSZ, where most of  
81 earlier studies have focused so far. This apparent rigidity resulted in contrasting  
82 interpretations regarding strain distribution and exhumation mechanisms. Although this major  
83 structure has probably accommodated a significant part of the finite deformation, the internal  
84 deformation and its evolution toward the ETSZ have never been fully described.

85 In this study, we reviewed the style, magnitude, and significance of deformation of the  
86 entire Tenda massif based on a new and extensive structural characterization. Finite strain  
87 markers relative to burial and exhumation were identified, mapped and characterized across a  
88 large portion of this continental unit. A scale of relative strain intensity and partitioning in the  
89 eastern granitic complex of the Tenda massif was built with the aim to reconstruct a  
90 succession of superimposed structures in a continuum of deformation. Thus, a new high  
91 resolution map of the intensity of deformation is here presented, having implications on strain  
92 distribution, strain localization factors and exhumation processes during the whole  
93 subduction/exhumation story.

94

## 95 2. Geological setting

96

### 97 2.1. Alpine Corsica

98

99 Corsica is divided in two geological domains: Variscan Corsica in the west and Alpine  
100 Corsica in the northeast (Durand-Delga, 1984) (Fig. 1). Alpine Corsica consists of a stack of

101 variably metamorphosed tectonic units belonging to a *HP-LT* subduction complex (e.g.  
102 Mattauer et al., 1981; Lahondère, 1988; Fournier, 1991; Caron, 1994; Vitale Brovarone et al.,  
103 2013). Formerly attached to the European continent, Corsica and Sardinia have migrated  
104 during the rifting of the Liguro-Provençal basin to reach their current position in Oligocene-  
105 Miocene times (e.g. Réhault et al., 1984; Speranza et al., 2002; Ferrandini et al., 2003;  
106 Maffione et al., 2008). Although multiple tectonometamorphic units can be distinguished (e.g.  
107 Vitale Brovarone et al., 2013), Alpine Corsica is conventionally divided into three major  
108 groups of units, from bottom to top: 1 - the external continental units, including the Tenda  
109 massif; 2 - the Schistes Lustrés nappe; and 3 - the Nappes Supérieures (Durand-Delga, 1984;  
110 Jolivet et al., 1990; Malavieille et al., 1998; Molli, 2008) (Fig. 1).

111         The external continental units correspond to autochthonous or parautochthonous units  
112 that were involved in Alpine subduction under greenschists to lower blueschists-facies  
113 conditions for the Sampolo and Popolasca units (Malasoma et al., 2006; Malasoma and  
114 Marroni, 2007; Garfagnoli et al., 2009; Vitale Brovarone et al., 2013; Di Rosa et al., 2016) up  
115 to middle-grade blueschists-facies conditions for the Tenda massif (Gibbons and Horak, 1984;  
116 Tribuzio and Giacomini, 2002; Molli and Tribuzio, 2004; Maggi et al., 2012; Vitale  
117 Brovarone et al., 2013).

118         The Schistes Lustrés nappe is mainly composed of more or less coherent pieces of  
119 metabasites, metasediments of oceanic affinity and few subordinate continental units (Centuri  
120 and Serra di Pigno units). These continental slices were incorporated in the Schistes Lustrés  
121 complex during the Alpine subduction (Faure and Malavieille, 1981), or prior to subduction,  
122 as extensional allochthons, in an Ocean-Continental Transition zone (OCT) (Lahondère and  
123 Guerrot, 1997; Martin et al., 2011; Vitale Brovarone et al., 2011a; Meresse et al., 2012). The  
124 Schistes Lustrés nappe was deeply buried during subduction as evidenced by the widespread  
125 occurrences of blueschist- and eclogite-facies assemblages present in both internal continental

126 units and metabasites (Caron et al., 1981; Caron and Péquignot, 1986; Lahondère, 1988;  
127 Fournier et al., 1991; Caron, 1994; Jolivet et al., 1998; Ravna et al., 2010; Vitale Brovarone et  
128 al., 2011a; 2011b).

129 The Nappes Supérieures (Balagne, Nebbio, Macinaggio, Pineto and Inzecca units)  
130 essentially consist of ophiolites of Jurassic age and Cretaceous flyschs of Ligurian affinity  
131 (Beccaluva et al., 1981; Ohnenstetter et al., 1981; De Wever et al., 1987) of low metamorphic  
132 grade (i.e.  $T_{\max} = 300$  °C, Vitale Brovarone et al., 2013).

133 These nappes are overthrust on the autochthonous crystalline basement of Variscan  
134 Corsica and Eocene foreland deposits (Fig. 1) ensuring a Bartonian biostratigraphic constraint  
135 on the timing of Alpine deformation at the front of the belt (Bonnal et al., 1973; Bézert and  
136 Caby, 1988; Jourdan, 1988; Egal and Caron, 1989; Vitale Brovarone et al., 2013). *HP-LT*  
137 metamorphism in the Schistes Lustrés nappe yielded scattered ages spanning from  
138 controversial Late Cretaceous ages (Sm-Nd on whole-rock, garnet, jadeite and glaucophane,  
139 Lahondère and Guerrot, 1997;  $^{40}\text{Ar}/^{39}\text{Ar}$  on glaucophane, Maluski, 1977) to Late Eocene ages  
140 ( $^{40}\text{Ar}/^{39}\text{Ar}$  on phengite, Brunet et al., 2000; U-Pb on zircon, Martin et al., 2011; Lu-Hf on  
141 Garnet; Vitale Brovarone and Herwartz, 2013). *HP-LT* rocks from the Tenda massif yielded  
142 almost similar ages from  $54 \pm 8$  Ma (U-Pb on acmite-phengite assemblages, Maggi et al.,  
143 2012) and  $\sim 36$  Ma ( $^{40}\text{Ar}/^{39}\text{Ar}$  on phengite, Brunet et al., 2000). Similar ages (37-33 Ma) were  
144 retrieved from the most external Alpine shear zones ( $T = 300$ °C;  $P > 0.6$  GPa) affecting the  
145 Variscan basement ( $^{40}\text{Ar}/^{39}\text{Ar}$  on phengite; Di Vincenzo et al., 2016).

146 Timing of exhumation and extensional tectonics appears also quite well constrained.  
147 Extensional regime is ensured by the development of extensional sedimentary basins that  
148 overprinted the structure of the subduction complex, notably the St-Florent basin that  
149 developed on top of the Nebbio and the Schistes Lustrés nappe. Activity of the bounding  
150 normal faults is ascribed to the syn-tectonic deposition of Burdigalian to Serravallian marine

151 sediments (Ferrandini et al., 1998; Cavazza et al., 2007). Besides, the youngest retrogression  
152 ages associated to exhumation retrieved from greenschist-facies rocks are well constrained in  
153 both the Schistes Lustrés nappe and the Tenda massif between 25 and 20 Ma (Brunet et al.,  
154 2000; Rossetti et al., 2015). Final exhumation stages of the internal zones including the Tenda  
155 massif as constrained by fission tracks low-temperature thermochronology on both zircon and  
156 apatite yielded Late Oligocene to Miocene ages (Jakni et al., 2000; Fellin et al., 2006).

157         At first glance, the finite structure of Alpine Corsica therefore results from a quite  
158 simple two-stepped tectonometamorphic evolution of subduction (burial) and exhumation.  
159 The first event corresponds to ductile deformation recorded in *HP-LT* conditions in both the  
160 Schistes Lustrés and Tenda units. This event is associated with a top-to-the-SW shearing  
161 localizing toward the contact between the two units that accommodated the thrusting of the  
162 Schistes Lustrés nappe over the Tenda massif (Cohen et al., 1981; Faure and Malavieille,  
163 1981; Mattauer et al., 1981; Jourdan, 1988; Molli and Tribuzio, 2004; Molli et al., 2006). It  
164 is followed by a post-*HP* event including series of top-to-the-E shearing and E-verging  
165 folding extensional increments in the Schistes Lustrés nappe (Faure and Malavieille, 1981;  
166 Jolivet et al., 1990; 1991; Fournier et al., 1991) and the Tenda massif (Jourdan, 1988; Jolivet  
167 et al., 1990; 1991; Daniel et al., 1996; Molli and Tribuzio, 2004; Molli et al., 2006). These  
168 late structures were interpreted as reactivating in the opposite direction some early thrusts  
169 either as backthrusts (Faure and Malavieille, 1980), or as extensional shear zones (Jolivet et  
170 al., 1990; 1991; Fournier et al., 1991; Daniel et al., 1996; Molli and Tribuzio, 2004; Molli et  
171 al., 2006; Rossetti et al., 2015). Interpreted as the result of syn-orogenic extension or regional  
172 post-orogenic extension, the geodynamic context that prevailed during early stages of  
173 exhumation is a matter of debate, leaving interpretation of some first order contacts, such as  
174 the ETSZ, controversial (Molli et al., 2006).

175

## 176 2.2. The Tenda massif and the ETSZ

177

178 The Tenda massif (Fig. 1) is bounded to the east by the ETSZ that marks the contact  
179 with the Schistes Lustrés nappe and to the west by the Ostriconi fault, which instead puts it in  
180 contact with the Nappes Supérieures of Balagne (Jourdan, 1988). It consists primarily to a  
181 Variscan basement portion overlain by Meso-Cenozoic cover series all involved into Alpine  
182 tectono-metamorphic events (Fig. 2). To the west, it is represented by Proterozoic to  
183 Paleozoic medium-grade rocks (gneisses and micaschists) unconformably overlain by Late  
184 Variscan volcano-sedimentary rocks (Rossi et al., 1994). At variance, the eastern part of the  
185 massif is mainly composed of a Late Carboniferous-Early Permian granitic complex (Rossi et  
186 al., 1993), intrusive in the volcano-sedimentary rocks. It includes from east to west the Mt  
187 Asto monzogranite, directly under the Schistes Lustrés nappe, the Casta granodiorite and the  
188 Mt Genova leucomonzogranite, in contact with the volcano-sedimentary and micaschists  
189 sequences (Rossi et al., 1994). The Triassic to Eocene sedimentary cover that remains united  
190 with the basement is only locally preserved, notably near Santo-Pietro-di-Tenda in the east  
191 (Jourdan, 1988; Rossi et al., 2001; Vitale Brovarone et al., 2013).

192 Evidence of the Alpine subduction of the Tenda massif is expressed by both an intense  
193 deformation near the ETSZ and the local development of *HP-LT* index metamorphic  
194 associations. They are often limited to celadonite-rich phengite in all types of intrusive rocks,  
195 and sodic blue-amphibole (riebeckite-ferroglaucophane), jadeite-bearing aegirine or even  
196 clinopyroxene + rutile, in granitoids of peculiar composition (Gibbons and Horak, 1994;  
197 Tribuzio and Giacomini, 2002; Molli and Tribuzio, 2004; Molli et al., 2006; Maggi et al.,  
198 2012; Rossetti et al., 2015). Peak metamorphic conditions estimates fall in the blueschists-  
199 facies conditions in the range of 1-1.2 GPa and 400-450 °C (Tribuzio and Giacomini, 2002;  
200 Molli and Tribuzio, 2004; Molli et al., 2006; Maggi et al., 2012) confirmed by independent

201 temperature estimates retrieved on metasediments from cover series (Vitale Brovarone et al.,  
202 2013). Exhumation is marked by an overall pressure decrease inferred from the decrease in  
203 Si-content in phengite (Molli et al., 2006; Maggi et al., 2012; Rossetti et al., 2015). An  
204 exhumation path was recently recognized from ~1 GPa and 450 °C to < 0.5 GPa and 300-  
205 400°C (Tribuzio and Giacomini, 2002; Molli and Tribuzio, 2004; Molli et al., 2006).

206 Just as the whole Alpine Corsica, the finite structure of the Tenda massif was achieved  
207 through a two-stepped history. All studies agree on a first event,  $D_1$ , responsible for the  
208 development of a first planar-linear fabric (referred as  $S_1/L_1$  in this study) accompanied with  
209 a top-to-the-SW sense of shear during subduction and burial in blueschists-facies conditions  
210 (Cohen et al., 1981; Mattauer et al., 1981; Jourdan, 1988; Daniel et al., 1996; Molli and  
211 Tribuzio, 2004; Molli et al., 2006; Molli and Malavieille, 2011; Maggi et al., 2012; 2014;  
212 Rossetti et al., 2015). This event corresponds to the underthrusting of the Tenda massif below  
213 the Schistes Lustrés nappe. Except for  $D_1$ , models and history of subduction/exhumation and  
214 strain localization of the Tenda massif in the frame of Alpine Corsica can be very different  
215 depending on papers. Three models are proposed:

216 - For Jolivet et al. (1990; 1991), Daniel et al. (1996) and Gueydan et al. (2003),  $D_1$  is  
217 placed during the Eocene. Then, a post-orogenic exhumation of Alpine Corsica started near  
218 30 Ma, with top-to-the-NE deformation localized notably toward the ETSZ that is reworked  
219 in greenschist-facies conditions. This  $D_2$  phase is associated to folds affecting the former  $S_1$ ,  
220 and a crenulation cleavage (referred as  $S_2$  in this study) preserved in less non-coaxial  
221 deformation domains between top-to-the-NE shear zones. A second lineation (referred as  $L_2$   
222 in this study) developed on  $S_2$  planes. The feldspar-to-phengite reaction is responsible for  
223 strain localization near the contact with the Schistes Lustrés nappe (Gueydan et al., 2003). A  
224  $D_3$  phase is used in this model for brittle extensional structures in a continuum of deformation  
225 during exhumation (Daniel et al., 1996).

226 - A more recent model rather considers most of the exhumation syn-orogenic (Molli  
227 and Tribuzio, 2004; Molli et al., 2006). The  $D_1$  phase is therefore placed earlier, before the  
228 Early Eocene and until  $\sim 40$  Ma.  $S_1$  folding and crenulation cleavage are interpreted occurring  
229 in low-strained domains in between zones of localized top-to-the-SW shearing during  $D_1$   
230 (Molli et al., 2006; Rossetti et al., 2015). After  $\sim 40$  Ma, during thrusting of the most external  
231 continental domains, a first step of syn-convergence exhumation ( $D_2$ ) occurred for both the  
232 Schistes Lustrés nappe and the Tenda massif until  $\sim 32$  Ma. It is accommodated by a top-to-  
233 the-SW shear zone contact below the Tenda massif and a top-to-the-NE shear zone at the top  
234 of the Schistes Lustrés nappe (Molli and Tribuzio, 2004; Molli et al., 2006). Associated  
235 structures are  $D_2$  folds, crenulation and both top-to-the-NE and -SW shear bands formation in  
236 the Tenda massif, and penetrative folding in the Schistes Lustrés nappe. The contact between  
237 the two units is itself involved in large-scale  $D_2$  folds, in a general delocalization of strain  
238 within the orogenic wedge. The ETSZ is finally reactivated in a post-orogenic context until  
239 brittle conditions at the end of the exhumation ( $D_3$ ). Those final phases of exhumation  
240 evolved from the ductile field (top-to-the-NE shearing and folds with axes parallel to the  
241 stretching lineation) up to the brittle field, with the development of semi-brittle shear bands  
242 and cataclasite-bearing fault zones.

243 - A third model (Maggi et al., 2012; 2014; Rossetti et al., 2015) is in agreement with  
244 the timing of events and the syn-orogenic character of exhumation described in the previous  
245 model of Molli and Tribuzio (2004) and Molli et al. (2006). However, the ETSZ remained  
246 active during exhumation with progressive strain localization from distributed in gneiss lenses  
247 to localized in top-to-the-SW shear zones. The ETSZ is characterized by a transient rheology  
248 with softening during feldspar-to-micas reaction and hardening by neoblastesis of K-feldspar  
249 during fluid metasomatism. The ultimate stage of localization is top-to-the-SW phyllonites,

250 which are the only structures reactivated semi-brittlely during post-orogenic extension. In  
251 their model, the Tenda massif remains undeformed beneath the ETSZ.

252

### 253 3. Structure and finite strain of the Tenda massif

254

255 A field survey was carried out on the whole Tenda massif including a detailed study of  
256 structural features and geological mapping in order to complement the map of the French  
257 Geological Survey (BRGM; Rossi et al., 1994; 2001). Strain markers were retrieved over  
258 more than 700 measurement stations throughout the massif. In the deformed parts, all  
259 metamorphic rocks are often pervasively foliated and generally exhibit a well-defined  
260 stretching lineation. Results are projected on the maps of figures 2 (foliations) and 4  
261 (stretching lineations with sense of shear) and are illustrated by representative outcrops and  
262 cross sections (Figs. 3 and 5), complementing earlier studies focused on the ETSZ (Daniel et  
263 al., 1996; Molli and Tribuzio, 2004; Molli et al., 2006; Maggi et al., 2014).

264

#### 265 3.1. Foliations and folds

266

267 At least two planar fabrics, related to  $D_1$  and  $D_2$ , are observed, some forming large-  
268 scale features apparent in the landscape (Fig. 3). A total of 207  $S_1$  and 482  $S_2$  planes were  
269 measured in all lithologies of the Tenda massif and in the Schistes Lustrés nappe close to the  
270 contact (Fig. 2a). Both  $S_1$  and  $S_2$  are found in almost the whole volume of the massif showing  
271 that deformation is not restricted to the ETSZ.  $S_2$  commonly dips away from the center of the  
272 Tenda massif with trajectories showing a concentric pattern depicting a N140°E elongated  
273 structural dome (Fig. 2). The apparent prevalence of NE-dipping planes is due to  
274 oversampling of  $S_2$  planes within the ETSZ.  $S_1$  planes show instead a N170°E preferred

275 orientation (Fig. 2).  $S_2$  generally displays dips between 0 and 45° with very low dispersion  
276 (Fig. 2c).  $S_1$  dip shows instead a higher dispersion (from 0 to 90°) depending on the degree of  
277  $D_2$  reworking. Structural relationships between  $S_2$  and  $S_1$  were studied in detail along the main  
278 road from St-Florent to Bocca di Vezzu (see location on Fig. 2a). Deformation appears  
279 heterogeneously distributed with lenses-shaped domains associated to rocks showing no or  
280 only a weak record of  $D_2$  deformation (see grey domains in Fig. 2b) and surrounded by  
281 anastomosed  $D_2$  corridors (see  $S_2$  trajectories in Fig. 2b). Low-strain domains consist in lense-  
282 shaped volumes of both unstrained Variscan magmatic rocks and weakly deformed facies,  
283 with incipient flat to gently dipping  $S_1$ . The largest one occurs in the core of the Tenda massif  
284 and roughly corresponds to the cartographic outline of the Casta granodiorite (Fig. 2). When  
285 weakly reworked by  $D_2$ ,  $S_1$  exhibits small- to large-scale undulations (Fig. 3a). With  
286 increasing  $D_2$  reworking,  $S_1$  is involved into recumbent isoclinal  $D_2$  folds whose axial planes  
287 correspond to shallowly dipping  $S_2$  crenulation cleavage (Figs. 3b and 3c). Both  $S_1$  and  $S_2$   
288 carry a mineral association mainly made of quartz, albite and phengite in most granites, but in  
289 more mafic facies, blue-amphiboles highlight the folded  $S_1$ , and is retrogressed into chlorite in  
290  $S_2$  cleavage (Fig. 3d). In those typical outcrops characterized by  $D_2$  folds, envelopes of  $S_1$  are  
291 steeply dipping and strike NNW-SSE while  $S_2$ , in the same range of strike, is shallowly  
292 dipping (Fig. 3e). The associated  $D_2$  folds axes also trend NNW-SSE with gently dipping  
293 plunges.

294         With increasing  $D_2$  strain intensity,  $S_1$  can be almost completely transposed into the  $S_2$   
295 fabric, especially along the Saleccia Shear Zone (SSZ) and the ETSZ where it can be  
296 observed at landscape-scale (Figs. 3f and 3g, respectively). The uppermost structural levels of  
297 the ETSZ show a single  $S_2$  fabric that is itself involved in metric to decametric recumbent  
298 isoclinal folds in a progressive  $D_2$  deformation (i.e. the  $D_3$  folds of Molli et al., 2006). The  
299 geometry of these late  $D_2$  folds evolves from open recumbent folds to overturned, then to

300 sheath folds, with trends axes evolving from NW-SE to ENE-WSW (Figs. 3h and 3i),  
301 parallelizing to the local stretching (Fig. 4). Dimensions of  $D_2$  folds across the massif vary  
302 from a few centimeters to several tens of meters.

303

### 304 3.2. Stretching lineations

305

306 Stretching lineation is defined by various markers, depending primarily on the nature  
307 of the protolith and the strain intensity. For both  $D_1$  and  $D_2$ , stretching lineation is marked in  
308 granites by stretched quartz rods, truncation of feldspar, strain shadows, and more commonly  
309 by elongated phyllosilicate aggregates such as phengite. Similarly, stretching lineation is  
310 conspicuous in metasediments. It is marked by fine-grained slates of phyllosilicates in pelitic  
311 layers or by the elongation of stretched pebbles in metaconglomerate layers. More rarely, it is  
312 marked by the alignment and truncation of prismatic minerals such as blue-amphiboles. In  
313 most outcrops, the orientation of the various types of lineation is fairly constant. Just as  $S_2$ ,  $L_2$   
314 is ubiquitous across the massif but is particularly marked in the vicinity of the ETSZ and  
315 second-order shear zones. Conversely,  $L_1$  is only locally expressed and restricted to low-strain  
316 domains.

317 A total of 166  $L_1$  and 408  $L_2$  orientations have been measured in all lithologies across  
318 the Tenda massif (Fig. 4a).  $L_1$  planes were only measured where they have not been  
319 verticalized during  $D_2$ . Trend and plunge of the different stretching lineations are almost  
320 comparable and show low dispersion (Fig. 4b) with a mean orientation of  $N050^\circ E-N060^\circ E$   
321 and a dominant NE-plunge related to the oversampling of  $S_2/L_2$  fabrics within the ETSZ.  
322 However, a slight yet reproducible difference in trends can however be detected at the scale of  
323 the outcrop. Consistent with the overall dome geometry, both  $L_1$  and  $L_2$  lineation mostly

324 plunge to the northeast in the northeastern flank and to the southwest in the southwestern  
325 flank.

326

#### 327 4. Kinematics of the polyphased deformation

328

329 Kinematics of deformation recorded in the Tenda massif is complex and characterized  
330 by the progressive overprint of opposing shear senses. The early subduction-related top-to-  
331 the-SW deformation is largely overprinted by the late top-to-the-NE extensional shear that  
332 prevailed during exhumation (e.g. Mattauer et al., 1981; Jolivet et al., 1990; 1991; Fournier et  
333 al., 1991; Daniel et al., 1996; Gueydan et al., 2003; Molli and Tribuzio, 2004; Molli et al.,  
334 2006; Maggi et al., 2012, 2014; Rossetti et al., 2015). In this section,  $D_2$  features are analyzed  
335 first and  $D_1$  next in order to properly unfold the sequence of top-to-the-NE and SW-directed  
336 deformations and adequately characterize their relative contribution to the finite geometry of  
337 the massif.

338

##### 339 4.1. Description and distribution of top-to-the-NE deformation ( $D_2$ )

340

341 Top-to-the-NE deformation is heterogeneously distributed within the Tenda massif  
342 (Figs. 4a and 5). It concentrates, at the first glance, toward the higher parts of the dome in the  
343 vicinity of the ETSZ and therefore mantles a relatively less deformed core preserving  $D_1$   
344 features (Fig. 5a). This deformation is spectacularly exposed within the northern outcrop of  
345 the ETSZ where a ca. 200 m-thick NE-dipping mylonites are classically described (Jolivet et  
346 al., 1990; 1991; Fournier et al., 1991; Daniel et al., 1996; Gueydan et al., 2003; Molli and  
347 Tribuzio, 2004; Molli et al., 2006; Maggi et al., 2012, 2014; Rossetti et al., 2015). Due to the  
348 dome-shaped architecture of the Tenda massif, top-to-the-NE deformation displays gentle to

349 moderate northeastward dips and normal-sense relative displacements on the northeastern  
350 flank of the dome while it often presents flat or even “reverse” geometry on the southwestern  
351 flank in the vicinity of the Ostriconi fault (Fig. 5a). This first-order geometry hides smaller-  
352 scale yet abundant top-to-the-NE structures that are particularly relevant for the discussion.  
353 Those observations are projected along the synthetic cross section presented in Fig. 5.

354 First, top-to-the-NE deformation also concentrates toward another shear zone of prime  
355 importance, the Saleccia Shear Zone (SSZ) that is described for the first time in this study (see  
356 Fig. 3f). There,  $D_2$  deformation occurs within granitoids roughly 1 km structurally below the  
357 ETSZ and evolves upward from gently NE-dipping protomylonites preserving  $D_1$  subvertical  
358 fabrics, to mylonites and ultimately rare stripes of ultramylonite bodies over a ca. 150 m-thick  
359 strain gradient where deformation localizes within the Saleccia rhyolite (Fig. 5b). In this  
360 gradient, the mylonitic  $S_2$  strikes NW-SE and moderately dips to the northeast (Fig. 3f). In the  
361 most deformed domains of the SSZ, spacing between  $D_2$  shear bands is locally as low as 0.5  
362 to 1 cm (Fig. 5b) and it increases downward, leaving lens-shaped domains where  $S_1$  is  
363 preserved.

364 Top-to-the-NE deformation also occurs as 10-50 cm-thick localized shear zones that  
365 rework previous fabrics or even undeformed protolith. Within the most deformed rock  
366 volumes, spacing between shear bands is locally as dense as 1-2 cm. Away from the core of  
367 shear zones, asymmetry and more generally imprint of  $D_2$  deformation decreases over a short  
368 distance (Fig. 5c). Locally, shear zones at high angle with respects to the main foliation  
369 suggest a brittle component during top-to-the-NE deformation (Fig. 5d). These narrow shear  
370 zones are consistently NE-dipping from the west to the east of the Tenda massif (Figs. 5a, 5c  
371 and 5d), crosscutting the large-scale dome structure.

372 In various lithologies cropping out in the west (i.e. volcano-sedimentary rocks), shear  
373 bands are the most ubiquitous shear-sense indicators. There, competent objects (i.e. remnants

374 of compositional layering or dykes) are asymmetrically boudinaged within more ductile  
375 metapelites. On the main D81 road, lenses of meta-rhyolite intrusions display a sigmoidal  
376 internal  $S_2$  foliation consistent with an overall top-to-the-NE sense of shear (Fig. 5e). In the  
377 bulk of those intrusions, the  $S_1/L_1$  fabrics are involved in recumbent isoclinal  $D_2$  folds with  
378 the development of a  $S_2$  crenulation cleavage with a low ( $\sim 20^\circ$ ) westward dip (Fig. 5f).

379 The reactivation of pre-existing shallow-dipping discontinuities also occurs in the  
380 vicinity of the intrusive contact between the western granitic complex and the volcano-  
381 sedimentary country-rocks. Such is the case at the Punta di Mignola (see Fig. 2 for location)  
382 where top-to-the-NE mylonites occur as a 20 m-thick shear zone that overprints the primary  
383 intrusive contact that is preserved as partially transposed granitic dykes asymmetrically  
384 boudinaged within the metasedimentary matrix (Fig. 5g). Despite the preservation of primary  
385 intrusive boundaries, their igneous protolithic texture is hardly recognizable. Here again,  
386 shear bands present an apparent flat/reverse geometry.

387 Due to the scarcity of index minerals in most of the rocks, the physical conditions that  
388 prevailed during top-to-the-NE deformation are not easy to retrieve continuously. In the most  
389 mafic lithologies, top-to-the-NE shearing can be associated with the boudinage or even the  
390 truncation of blue-amphiboles (Figs. 5h and 5i). In these rocks, a second generation of small-  
391 scale blue-amphibole can occur during this  $D_2$  stretching but gaps between the fragments of  
392 large blue-amphiboles and along the top-to-the-NE shear bands are mostly recorded during  
393 crystallization of chlorite (Fig. 5i). In more felsic granitic lithologies that represent most of  
394 the Tenda massif, the top-to-the-NE mylonites of the ETSZ are made of quartz, albite and  
395 phengite that are sometimes associated with chlorite and pyrite (Fig. 5j).

396

397 4.2. Description and distribution of top-to-the-SW deformation ( $D_1$ )

398

399 Top-to-the-SW deformation is located in the same structural level as rocks only  
400 affected by  $S_1$  that wrap unstrained Variscan magmatic rocks (compare Figs. 2b and 4a).  
401 Study of top-to-the-SW deformation has therefore been restricted to the exploration of the  
402 lower parts of the dome along sections showing the upward development of  $S_1$  and the  
403 associated simple shear markers at the expense of the Variscan magmatic protoliths.

404 In the core of the less deformed domains (Fig. 2b), the inherited Variscan magmatic  
405 paragenesis including K-feldspar, plagioclase, quartz, biotite and hornblende is metastably  
406 preserved within incipient coronitic reactions. Among the most obvious reactions, hornblende  
407 is statically transformed to blue-amphibole. These domains, which display no perceptible  
408 deformation, are surrounded by rocks affected by  $S_1/L_1$  tectonites. While the base of this  
409 strain gradient is dominated by less non-coaxial deformation, it rapidly evolves toward top-to-  
410 the-SW simple shear deformation marked by the development of a single set of shear bands  
411 (Figs. 4a and 5a). Besides, this strain gradient is further complicated by more local strain  
412 localization, even at the scale of a single outcrop, as exemplified by the base of the ETSZ, along  
413 the main D81 road (Figs 6a, 6b, 6c). Here, top-to-the-SW deformation can occur as localized  
414 shear bands that overprint a volume of rocks devoid of visible deformation (Fig. 6a). In this  
415 case,  $S_1$  only develops near shear bands and passes laterally to the undeformed protolith.  
416 Shear bands can also work as limits between isotropic granite on one side and oblique  $S_1$  on  
417 the other side. Those observations suggest that prior or during formation of  $S_1$ ,  $D_1$  deformation  
418 started along discrete precursors in the form of shear bands. In this case, the flat orientation of  
419 shear bands appears controlled by the orientation of the precursor. Within the most deformed  
420 volumes of this outcrop,  $D_1$  deformation is more distributed, with regularly spaced top-to-the-  
421 SW shear bands with  $S_1$  sigmoidal (Fig. 6b). In this context, typical spacing between shear  
422 planes varies between 1 and 3 cm, depending on the size of magmatic K-feldspar clasts, and  
423 they dip to the west.  $S_1$  appears generally flat, highlighted by stretched quartz ribbons

424 alternating with feldspar ribbons. The most deformed parts of this outcrop are concentrated in  
425 a very gently dipping high strain shear band showing a fast lateral widening from less than  
426 1cm up to ~10 cm (Fig. 6c). Near the core of the ETSZ,  $D_1$  deformation is occasionally  
427 preserved from  $D_2$  as small-scale lens-shaped domains that often show internal mylonitic  
428 deformation (Fig. 6d). There, both the  $S_1$  and the top-to-the-SW shear planes show evidence  
429 of passive rotation as they now dip eastward. Field observations on those structural levels  
430 indicate that when both top-to-the-SW and -NE shear criteria coexist, the first ones are always  
431 crosscut by the second ones (Fig. 6e).

432 In granitic lithologies, physical conditions that prevailed during top-to-the-SW  
433 deformation are generally not easy to retrieve. Blue-amphiboles sporadically develop either  
434 along the  $S_1$  or along the top-to-the-SW shear bands. Conversely, more mafic lithologies, top-  
435 to-the-SW shearing appears clearly associated with the growth of synkinematic blue-  
436 amphiboles (Fig. 6d).

437

## 438 5. Mapping the state of finite deformation within the Tenda granites

439

### 440 5.1. Approach and methodology

441

442 Variably strained granite constitutes the dominant lithology in the east of the Tenda  
443 massif. Granitic protoliths appear well suited to determine local and regional variations in the  
444 magnitude of deformation, either qualitatively or quantitatively. Quantitative estimates as  
445 retrieved from image analysis (e.g. Launeau and Robin, 2005) or anisotropy of magnetic  
446 susceptibility analysis (e.g. Borradaile and Jackson, 2010) are valuable in such contexts but  
447 are often local in extent. To put constraints on the large-scale pattern of deformation ( $> 100$   
448  $\text{km}^2$ ), exhaustive mapping of the state of finite deformation has been applied qualitatively as

449 described in Huet et al. (2009), Charles et al. (2011), and Laurent et al. (2015). Laurent et al.  
450 (2015) have shown a good correlation between this qualitative approach and quantitative  
451 methods.

452 As discussed above, the effects of  $D_1$  and  $D_2$  can be generally unambiguously  
453 separated. The intensity of the  $D_2$  overprint, however, is locally so severe as to allow only the  
454  $D_2$  finite deformation pattern to be continuously mapped across the massif. Five strain grades  
455 were distinguished to describe the intensity of deformation across the protolith (Fig. 7).  
456 Geometric embedding of the different strain grades is presented on figure 8.

457 - Grade 0 corresponds to rocks that did not experience significant  $D_2$  deformation,  
458 such as  $D_2$  folds,  $S_2$ ,  $L_2$  or top-to-the-NE simple shear indicators. Within this grade, rocks may  
459 be either coarse grained or mylonitized during  $D_1$ . Thus, two sub-grades were distinguished.  
460 Grade 0s.s. corresponds to the undeformed protolith characterized by an equant fabric where  
461 blue-amphiboles can statically replace magmatic hornblende (Figs. 7a and 7b). Besides, grade  
462 0W corresponds to any other rocks deformed during  $D_1$  and showing typical features such as  
463 top-to-the-SW shear bands,  $S_1$  or  $L_1$  but no trace of  $D_2$  deformation (Fig. 7c).

464 - Grade 1 characterizes rocks that experienced incipient  $D_2$  deformation superimposed  
465 on  $D_1$  features. In the field, typical examples are outcrops showing  $D_2$  folds associated with  
466 two different fabrics: a steep and folded  $S_1$  and a sub-horizontal  $S_2$  crenulation cleavage (Figs.  
467 3b, 3c, 3d, 5f and 7d). There,  $S_1$  can be either gently folded or strongly crenulated. However,  
468 it shows in any case a pure shear component corresponding to subvertical shortening.  $D_1$  top-  
469 to-the-SW shear bands may be locally preserved associated with the sigmoidal character of  
470  $S_1$ . In those cases, top-to-the-SW shear bands and  $S_2$  planes have comparable orientations,  
471 suggesting that shear bands represented weak zone where  $S_2$  lately localized.

472 - Grade 2 is characterized by unequivocal top-to-the-NE simple shear indicators  
473 associated to asymmetric boudins and particularly to shear bands while  $D_2$  folds remain the

474 main feature. In some cases,  $S_2$  crenulation planes are used as shear bands (Fig. 7e). In this  
475 case,  $S_1$  is comprised and between  $S_2$  planes, indicating top-to-the-NE shearing. In other  
476 cases, newly formed top-to-the-NE shear bands affect a sigmoidal  $S_2$  (Fig. 7f). Angle between  
477 shear planes and foliation is about  $60^\circ$ .

478         Increasing degree of simple shear from grades 2 to 4 is then recorded by an overall  
479 decrease of both spacing between top-to-the-NE shear bands and the angle between the  $S_2$  and  
480 the shear bands, responsible for the progressive transposition of  $D_1$  structures (Figs. 7f to 7h).

481         - Transition between grades 2 and 3 is marked by the occurrence of top-to-the-NE  
482 shear bands that are regularly spaced between 5 and 10 cm, affecting a sigmoidal  $S_2$  (Fig. 7f).  
483 The angle between shear bands and foliation can be bracketed between  $30$  and  $60^\circ$ .  $D_2$  folds  
484 are more rarely preserved, and shear bands dominate.

485         - Transition between grades 3 and 4 is marked by a decreasing angle between top-to-  
486 the-NE shear bands and  $S_2$ , beneath  $30^\circ$  (fig.7g). This flattening of mylonites is responsible  
487 for nearly complete obliteration of  $D_2$  folds, rarely still visible, and the regular spacing of  
488 shear bands near 1 cm.

489         - Grade 4 corresponds to the most deformed volumes, being characterized by  
490 occurrence of ultramylonites and by the almost total transposition of  $S_2$  (Fig. 7h).

491         The increase of finite strain intensity is therefore associated with a progressive  
492 increase of the simple shear component of deformation, from vertical shortening and folding  
493 of  $S_1$  to top-to-the-NE simple shear deformation. In this frame, the angle between top-to-the-  
494 NE shear planes and  $S_2$  progressively closes with the progressive reworking of the remaining  
495  $D_1$  structures (Fig. 8).

496

497 5.2. Grade distribution

498

499 Distribution of the deformation over the entire eastern Tenda massif was retrieved by  
500 applying this high-resolution strain intensity scale. In the cases of mixed grade for a same  
501 outcrop, overprinted structures (grade n-1) are generally boudinaged between anastomosed  
502 zones of overprinting structures (grade n). Local variations in deformation grade thus appear  
503 as snapshots of a continuum of deformation. This observation can be made at different scales  
504 (Fig. 9). To clarify the regional pattern, local mixed-grade stations are qualified with a single  
505 grade. Grade n-1 is chosen if it clearly represents a large part of the outcrop. For equal-  
506 proportion between grades n and n-1, grade n is chosen because it better represents the finite  
507 structure, as it appears as the latest phase. The resulting map, comprising 617 outcrops  
508 homogeneously distributed within the granitic complex, is shown on figure 10a. Four cross  
509 sections normal to the regional foliation and parallel to stretching are presented on figure 10b.

510 At the massif scale, the map shows that  $D_2$  affects a large part of the mapped area,  
511 except for the Casta granodiorite, which remains isotropic or only affected by  $D_1$  (cross  
512 sections BB' and DD' on Fig. 10). 75 % of the investigated outcrops are affected by  $D_2$ .  
513 Among those outcrops, 28 % are represented by grade 1 and 30 % by grade 2. Grades 3 and 4  
514 domains are of secondary importance, 24 % to 18 % respectively, a trend nicely indicating a  
515 localization of deformation with increasing finite strain. This distribution is shown both on the  
516 map and in the cross sections where the deformed zones become narrower with increasing  
517 strain intensity. At first-order, strain intensity clearly increases from west to east, toward the  
518 ETSZ (cross sections BB', CC', DD' on Fig. 10) and the SSZ (cross section AA' on Fig. 10).  
519 At a smaller scale, deformation zones also occur as isolated shear zones of moderate intensity  
520 (grade 2) in poorly deformed zones (grade 1) near Mt Genova (cross section BB' on Fig. 10).  
521 Similarly, isolated high-intensity shear zones (grade 4) occur in moderately deformed  
522 volumes within the ETSZ (cross section CC' on Fig. 10). The overall 3-D structure of the  
523 massif thus appears as a heterogeneous shear zone showing: i) a first-order strain gradient

524 toward the ETSZ and the SSZ, ii) isolated strain gradients at a smaller scale. As observed at  
525 different scales (Fig. 9), zones dominated by structures related to grade n-1 appear as lenses or  
526 boudins between zones affected by grade n (Fig. 10).

527

## 528 6. Discussion

529

530 Structural studies on the Tenda massif have been so far conducted on its eastern part,  
531 the ETSZ, an excellent example of polyphased contact accommodating both burial and  
532 exhumation of continental material (Daniel et al., 1996; Brunet et al., 2000; Gueydan et al.,  
533 2003; Molli and Tribuzio, 2004; Molli et al., 2006; Maggi et al., 2012; 2014; Rossetti et al.,  
534 2015). However, behavior of a large-scale continental crust portion and particularly strain  
535 accommodation of subduction and exhumation cannot be explored only by the detailed study  
536 of the major contacts where deformation is particularly concentrated. Our results show that  
537 deformation of the Tenda massif was not restricted to the ETSZ. Field results show the  
538 distribution of retrograde deformation related to exhumation and the pattern of partial to total  
539 transposition of the inherited top-the-SW fabric. One of the most important observation is that  
540 the later NE-directed (exhumation-related) structures are pervasively recorded across the  
541 entire massif. In the lights of these results, this section discusses the variation of strain  
542 distribution during burial and exhumation as well as the factors responsible for strain  
543 localization. Regional implications are presented first.

544

545 6.1. A review of the Tenda massif finite structure: regional implications on the model of  
546 subduction/exhumation

547

548           The various models of subduction and exhumation of the Tenda massif depend on: 1)  
549 the uncertain attribution of some structures to one of the different tectonic phases; 2) the focus  
550 of previous work on the ETSZ, that led to different descriptions of finite structure and patterns  
551 of strain distribution (Daniel et al., 1996; Brunet et al., 2000; Gueydan et al., 2003; Molli and  
552 Tribuzio, 2004; Molli et al., 2006; Maggi et al., 2012; 2014; Rossetti et al., 2015); 3) the  
553 scattering and various interpretation of chronological constraints. We discuss these three  
554 points in the next subsections.

555

556 6.1.1. To which deformation stage folds and crenulated structure belong?

557

558           Folds affecting  $S_1$  and associated to crenulation cleavage is differentially explained by  
559 the models presented in the section 2.2. They can develop in coaxial domain of deformation  
560 between top-to-the-NE shear zones during exhumation in greenschist-facies conditions  
561 (Jolivet et al., 1990; 1991; Daniel et al., 1996) or can occur in low-strained domains in  
562 between zones of localized top-to-the-SW shearing in blueschist-facies conditions (Molli et  
563 al., 2006; Rossetti et al., 2015). Our study shows that: 1) top-to-the-SW shearing can display  
564 different amounts of strain localization from distributed to strongly localized in a same  
565 outcrop without developing any crenulation (Fig. 6). 2) On the contrary, crenulation is rather  
566 localized where top-to-the-NE shearing occurs at outcrop scale (Figs. 5e, 5f, 7e, 7f and 9).  
567 This is also true for larger scales. For example, undulations of vertical  $S_1$  in the Mt Genova  
568 (Fig. 3a) occur in between two top-to-the-NE shear zones (Fig. 10). 3) This crenulation ( $S_2$ ) is  
569 associated to retrogression of blue-amphiboles, which developed in  $S_1$ , into chlorite,  
570 suggesting that  $S_1$  and  $S_2$  did not develop in the same  $P$ - $T$  conditions (Fig. 3d). For these  
571 reasons, we followed the model of Jolivet et al. (1990; 1991) and Daniel et al. (1996),  
572 according to which the crenulated structures are rather linked to  $D_2$ .

573 One important observation is that these folds are also observed in the eastern limb of  
574 the Cap Corse antiform (Fig. 1; Jolivet et al., 1991). There, the NE-verging recumbent folds  
575 are observed from a few centimeters to hundreds of meters and they are later sheared by top-  
576 to-the-E shear zones and cut by the brittle detachment observed near the northernmost tip of  
577 Cap Corse (Macinaggio detachment, Fig. 1). Thus, the two antiforms, namely the Tenda  
578 massif and the Cap Corse, show the same general asymmetry with a localized east-dipping  
579 shear zone at the top with folds overturned to the east underneath. This shows that these folds  
580 are not restricted to the Tenda massif but are instead characteristic of the late architecture of  
581 Alpine Corsica, including the Tenda massif and the Schistes Lustrés nappe as two separate  
582 crustal-scale boudins formed during extension (Daniel et al., 1996).

583

#### 584 6.1.2. Global strain distribution in the Tenda massif

585

586 In the frame of an orogenic wedge, the subduction/exhumation style and mechanism  
587 of continental material largely depends on the rheology of the subducting continental crust.  
588 To understand it, a careful structural description of pattern of strain distribution is needed.  
589 The fact that studies on those questions focused on the ETSZ leads sometimes to an apparent  
590 rigidity of the Tenda massif. Moreover, since the ETSZ is where the final increments of  
591 deformation toward the brittle field localized (Molli et al., 2006; Maggi et al., 2012; 2014),  
592 this focus leads to an overestimation of the relevance of brittle post-orogenic reactivation.  
593 Instead, our study shows that ductile markers of  $D_1$  ( $S_1$ ,  $L_1$ , top-to-the-SW shear criteria) and  
594  $D_2$  ( $S_2$ ,  $L_2$ , top-to-the-NE shear criteria) can be encountered from the ETSZ to the Ostriconi  
595 fault, except a few domains where the protolith remains unformed (notably the Casta  
596 granodiorite). In more details, the structural analysis of the Tenda massif (Fig. 5a) reveals a  
597 finite structure characterized by a ductile NW-SE dome of  $D_2$  features ( $D_2$  folds,  $S_2$ ,  $L_2$ , and

598 top-to-the-NE shear criteria) that rework  $D_1$  structures ( $S_1$ ,  $L_1$  and top-to-the-SW shear  
599 criteria). The relatively more deformed carapace mantles a less deformed core which can  
600 locally preserves undisturbed  $D_1$  structures. From west to east, this dome is crosscut by late  
601 top-to-the-NE narrow and localized shear zones that evolve toward a brittle behavior (Figs.  
602 5a, 5c and 5d). We then emphasize the fact that  $D_2$ , top-to-the-NE shearing, and switch of the  
603 ETSZ from a thrust to a detachment were mostly recorded in the ductile field, and pervasively  
604 affect the finite structure of the Tenda massif.

605

606 6.1.3. Geodynamic context for the exhumation of the Tenda massif

607

608 A major controversy exists about the respective part of regional compression and  
609 extension in the exhumation of the Tenda massif (see debate in Molli et al., 2006). The rather  
610 cold path of the exhumation favors a first step of syn-orogenic exhumation (Molli and  
611 Tribuzio, 2004; Molli et al., 2006; Maggi et al., 2012), also envisaged for more external  
612 continental units (i.e. the Popolasca unit for example; Malasoma and Marroni; 2007; Di Rosa  
613 et al., 2016). Instead, the end is clearly recorded during post-orogenic extension in  
614 greenschists-facies to brittle conditions, affecting the whole nappe stack (Molli and Tribuzio,  
615 2004; Molli et al., 2006; Malasoma and Marroni; 2007; Maggi et al., 2012; Di Rosa et al.,  
616 2016). Syn-orogenic exhumation may involve a thrust at the base and a detachment (or  
617 exhumation fault) at the top of the exhumed units (e.g. Chemenda et al., 1995; Raimbourg et  
618 al., 2005), whereas post-orogenic extension will rework the entire nappe stack. In the case of  
619 the Tenda massif, Molli et al. (2006) concluded that syn-orogenic exhumation has been  
620 responsible for most of the exhumation below the detachment situated between the Schistes  
621 Lustrés nappe and the Nappe Supérieures and accommodated by a thrust at the base of the  
622 Tenda massif. Unfortunately, this structural architecture cannot be proven because the basal

623 contact of the Tenda massif does not crop out anywhere (Fig. 5a). Only chronological  
624 constraints permit to discuss this problem (see Fig. 11).

625 A regional shift from compression to extension has been widely recognized from the  
626 Gulf of Lion to the Calabrian Arc in connection with the southeastward retreat of the  
627 Apennine slab (e.g. Malinverno and Ryan, 1986; Doglioni, 1991; Gueguen et al., 1998;  
628 Jolivet et al., 1998; 2008; 2015; Séranne, 1999; Brunet et al., 2000; Rossetti et al., 2001;  
629 Speranza et al., 2002; Faccenna et al., 2004). As attested by evidences of compression in Late  
630 Eocene-Early Oligocene sedimentary rocks of Sardinia (Faccenna et al., 2002) and syn-rift  
631 sediments of Middle Oligocene to Aquitanian age (23-20 Ma) in the Gulf of Lion (e.g.  
632 Séranne, 1999; Oudet et al., 2010; Jolivet et al., 2015), the shift from compression to  
633 extension occurred in the Oligocene probably near the Late Rupelian (34-28 Ma). Similarly,  
634 syn-rift sediments formed during Late Oligocene-Aquitanian times in Corsica and Sardinia,  
635 prior to their anticlockwise rotation as a rigid block during the spreading of the Liguro-  
636 Provençal Sea (e.g. Faccenna et al., 2002; Speranza et al., 2002; Ferrandini et al., 2003).

637 Top-to-the-SW shearing in the Tenda massif is constrained between early Eocene for  
638 its prograde increments (U-Pb on acmite-phengite-coatings, Maggi et al., 2012) and Early  
639 Oligocene for its waning stage (Brunet et al., 2000; Rossetti et al., 2015). The end of top-to-  
640 the-SW shearing at this time is coherent with Late Eocene-Early Oligocene *HP-LT* peak ages  
641 in the more buried levels of the Schistes Lustrés nappe (Martin et al., 2011; Vitale Brovarone  
642 and Herwartz, 2013) and with the post-Bartonian *HP-LT* thrusting in the external domains  
643 (Bonnal et al., 1973; Bézert and Caby, 1988; Jourdan, 1988; Egal and Caron, 1989; Vitale  
644 Brovarone et al., 2013) that all constrain the beginning of syn-orogenic exhumation. Recent  
645  $^{40}\text{Ar}/^{39}\text{Ar}$  ages on Alpine shear zones developing in the eastern Variscan basement argue for a  
646 major shearing during *HP-LT* peak at 37-35 Ma, before exhumation near 32 Ma (Di Vincenzo  
647 et al., 2016). As a conclusion, the syn-orogenic exhumation of the relatively internal domain

648 of Alpine Corsica (i.e. Schistes Lustrés nappe and Tenda massif) is narrowly constrained  
649 between ~38-32 Ma that is a maximum limit for *HP-LT* peak in the Schistes Lustrés nappe  
650 and for thrusting in the external domain, and ~32-30 Ma, during exhumation of the entire  
651 Alpine Corsica, synchronously with the regional compression-extension switch. This could  
652 happen when Corsica passed from an east-dipping Alpine subduction to the back-arc domain  
653 of the west-dipping Apennine subduction system near 35-30 Ma (e.g. Molli and Malavieille,  
654 2011; Malusà et al., 2015).

655 The regional compression/extension switch is recorded by Rb-Sr (Rossetti et al., 2015)  
656 and  $^{40}\text{Ar}/^{39}\text{Ar}$  (Brunet et al., 2000) ages on phengite affected by  $D_1$  and  $D_2$  in both the Schistes  
657 Lustrés and the Tenda units. In the Tenda massif, crystallization or re-crystallization of  
658 relatively substituted  $D_1$  phengite ( $\text{Si}^{4+} \sim 3.5$  a.p.f.u) during deformation in samples  
659 characterized by top-to-the-W kinematics are dated between 32 and 27 Ma by the Rb-Sr  
660 method while the  $^{40}\text{Ar}/^{39}\text{Ar}$  one gives a minimum age of 35 Ma. The end of  $D_2$  deformation is  
661 recorded in highly deformed samples characterized by top-to-the-NE kinematics and  
662 relatively less substituted phengite ( $\text{Si}^{4+} \sim 3.3$  a.p.f.u) at 20 and 25 Ma by the Rb-Sr and  
663  $^{40}\text{Ar}/^{39}\text{Ar}$  methods, respectively. The same ages are recorded in strongly retrogressed samples  
664 of the Schistes Lustrés nappe during  $D_2$ . The systematic difference of 5 Ma observed between  
665 the two methods questioned their ability to precisely date the timing of deformation.  
666 Accordingly, the compression/extension switch is differentially constrained near 27 Ma  
667 (Rossetti et al., 2015) or 32 Ma (Brunet et al., 2000). Further investigation are needed to  
668 precisely constrain the absolute timing of deformation relative to the different events.  
669 However, the two datasets indicate that the relative time between the ends of the two events is  
670 about ~7 Ma, showing that post-orogenic movements probably accommodated a non-  
671 negligible part of the exhumation.

672

## 673 6.2. Styles of deformation and strain localization during burial and exhumation

674

675 Many studies on strain localization and shear zone development have focused on cases  
676 where  $P$ - $T$  conditions remained constant through deformation. The Tenda massif offers  
677 instead an example where the distribution of deformation can be studied through variable  $P$ - $T$   
678 conditions during a full burial/exhumation cycle.

679

680 6.2.1. Burial ( $D_1$  phase)

681

682 The presence of a Mesozoic to Eocene sedimentary cover resting unconformably on  
683 the Tenda massif (Jourdan, 1988; Rossi et al., 2001; Vitale Brovarone et al., 2013) shows that  
684 it was near the surface just before its burial, as the Alpine events in external units started  
685 during the Bartonian (40 Ma; Bonnal et al., 1973; Bézert and Caby, 1988; Jourdan, 1988; Egal  
686 and Caron, 1989; Vitale Brovarone et al., 2013). Then, blueschist-facies conditions are  
687 recorded during  $D_1$  as attested by crystallization of blue-amphibole along  $S_1$  (Figs. 3c and 3d)  
688 and top-to-the-SW shear bands (e.g. Molli et al., 2006). At large-scale, blue-amphibole occurs  
689 principally in the Mt Asto granite, within the ETSZ (Fig. 2), suggesting that its occurrence  
690 depends in part on chemical composition of the protoliths and that it is favored by  
691 deformation. Despite this observation, blue-amphibole also occurs statically in non-deformed  
692 facies of the Casta granodiorite (Fig. 7b). Within the Mt Genova granite, two occurrences  
693 have been observed (Fig. 2a), the first one along the main D81 road, in a fine-grained facies  
694 strongly localizing deformation and the second one in micaschists of the Punta di Mignola  
695 shear zone (Figs. 2a and 5g). Further south of our study area, blue-amphibole also occurs in  
696 the westernmost parts of the Tenda massif (Near Urtaca, Jourdan, 1988; Molli and Tribuzio,  
697 2004). The most reliable peak  $P$ - $T$  conditions constraints are provided by petrological studies

698 in peculiar lithologies, away from the ETSZ, in the gabbroic complex of Bocca di Tenda,  
699 south of the Tenda massif. Here, rhyolite with jadeite-bearing aegirine, Na-amphibole and  
700 celadonite-rich phengite (Tribuzio and Giacomini, 2002) and gabbro with Al-poor hornblende  
701 and celadonite-rich phengite (Molli and Tribuzio, 2004) constrain peak metamorphism near 1  
702 GPa and 450 °C. Similar results (1.2 GPa, 400 °C) are obtained in the ETSZ with a peculiar  
703 clinopyroxene + rutile assemblage (Maggi et al., 2012). All those results suggest that the  
704 Tenda massif recorded a global blueschists-facies condition during burial, and remained a  
705 relatively coherent unit.

706 Even if the early brittle structures relative to burial have been completely overprinted  
707 by the later ductile deformation, we propose that first stage of deformation was probably  
708 localized along brittle thrust precursor, as observed in the Corte slices further south (Jolivet et  
709 al., 1990). The following ductile *HP-LT*  $D_1$  deformation ( $S_1$ ,  $L_1$ , top-to-the-SW shearing) is  
710 on the contrary distributed at large scale, affecting a large volume of the Tenda massif, from  
711 the core where it can preserve its original geometry, to the top of the dome where it is lately  
712 overprinted (Figs. 5a and 12). Distributed deformation is evidenced by gneissic texture during  
713  $D_1$  (Maggi et al., 2012; 2014). At the scale of outcrop, we do not find any evidences of  
714 structures related to the brittle-ductile transition for  $D_1$ . However, in the less deformed  
715 volume, we found that  $S_1$  developed only along top-to-the-SW shear bands and passes  
716 laterally to the undeformed protolith (Fig. 6a). Those observations suggest that  $D_1$   
717 deformation started along discrete precursors in the form of shear bands prior or during  
718 formation of  $S_1$ . It is coherent with studies focusing on the nucleation of shear zones where  
719 the amount of later overprint is limited. They demonstrate that shear zones nucleate from  
720 discrete precursors such as brittle fractures (e.g. Mancktelow and Pennacchioni, 2005;  
721 Raimbourg et al., 2005; Goncalves et al., 2012; 2016; Sullivan et al., 2013), lithological  
722 contacts (e.g. Pennacchioni and Mancktelow, 2007) or simply microscopic heterogeneities at

723 mineral boundaries (e.g. Ingles et al., 1999). Finally, the top-to-the-SW shear bands are lately  
724 overprinted by brittle fractures, making the nature of the precursor uncertain. However, all  
725 those points argue for a first step of strain delocalization within the Tenda massif during  
726 burial and its first crossing through the brittle-ductile transition from surface up to blueschists-  
727 facies conditions.

728

#### 729 6.2.2. Exhumation ( $D_2$ phase)

730

731 Structures related to exhumation were mostly recorded in greenschist-facies  
732 conditions, while blue-amphiboles were turned into chlorite in  $S_2$  crenulation and top-to-the-  
733 NE shear bands (Figs. 3d and 5i). It seems reasonable that they developed from blueschists-  
734 facies conditions, in a  $D_1$ - $D_2$  continuum deformation. Indeed, Molli et al. (2006) described a  
735  $D_2$  crenulation made of fine grains of Na-amphibole showing an outward decrease of Al,  
736 compatible with a decreasing pressure, between microlithons with large Na-amphiboles. We  
737 also find blue-amphibole recrystallization in the tails of older blue-amphibole sigma clasts  
738 compatible with top-to-the-NE shearing (see white square in Fig. 5i). The exhumation path  
739 can be constrained from  $\sim 1$  GPa and 450 °C to  $< 0.5$  GPa and 300-400°C (Tribuzio and  
740 Giacomini, 2002; Molli and Tribuzio, 2004; Molli et al., 2006). The last increments of  
741 exhumation are recorded in the brittle field (Fig. 5d) in a continuum deformation, as the  
742 directions of both ductile and brittle stretching are consistent (Molli et al., 2006).

743 Right after the burial/exhumation switch, the first stages of  $D_2$  deformation are  
744 characterized by pervasive folding responsible for a general verticalization of  $S_1$  envelope  
745 (Figs. 2c, 3e, 5a and 12). Folding is expressed in low-strain  $D_2$  domain by gentle undulations  
746 of  $S_1$  (Fig. 3a) or inversely strongly crenulated  $S_1$  associated to a flat  $S_2$  cleavage (Figs. 3b, 3c,  
747 3d), compatible with a pure shear component of deformation corresponding to a subvertical

748 shortening. Larger-scale folds can be observed near Santo-Pietro-di-Tenda, where they affect  
749 the contact between the Tenda massif and the Schistes Lustrés nappe (Molli et al., 2006).  
750 Limbs of the Schistes Lustrés nappe incorporated into the ETSZ (see Punta di Cepo and  
751 Fornali Bay in Fig. 2) also suggest a folding of this contact. Irrespective of these variations in  
752 scale, this folding stage is observed throughout the Tenda massif affected by D<sub>2</sub>. In agreement  
753 with Molli et al. (2006), we argue for a general strain delocalization at the time of D<sub>2</sub>,  
754 responsible for the buckling and deactivation of the original thrust just before or after the D<sub>1</sub>-  
755 D<sub>2</sub> switch (Fig. 12). Then, the strain intensity map shows that deformation is localized in  
756 narrower top-to-the-NE shear zones that locally develop thick mylonites and locally  
757 ultramylonites (Figs. 5, 7, 8 and 10). Furthermore, the transition from grade n-1 to n is marked  
758 by relatively poorly deformed boudins in a more deformed matrix (Fig. 9). Local variations in  
759 deformation grade thus appear as snapshots of a continuum of deformation that finally  
760 localized in the ETSZ and the SSZ, showing that D<sub>2</sub> deformation progressively localized  
761 during exhumation toward the two principal shear zones. This interpretation is further  
762 supported by the decrease of <sup>40</sup>Ar/<sup>39</sup>Ar ages on phengites toward the ETSZ nappe from ~45 to  
763 25 Ma (Brunet et al., 2000). Since the ductile structures are lately crosscut by NE-striking  
764 faults, the spatial and temporal relationships between the ETSZ and the SSZ are unclear.  
765 Further studies should better assess both brittle kinematics and provide radiometric  
766 chronological constraints also for the SSZ. In any case, the ETSZ and the SSZ are two  
767 different structures, the ETSZ developing at the top of the Tenda massif while the SSZ is  
768 structurally below and developed within the granitic complex (Fig. 10). Moreover, the two  
769 shear zones are characterized by different stretching directions, NE-SW for the ETSZ and  
770 NNE-SSW for the SSZ (Fig. 4a). Doming of the Tenda massif occurred during the  
771 progressive strain localization toward the ETSZ as the D<sub>2</sub> mylonites carapace near the top of  
772 the massif is itself domed and outcrops in the west (Fig. 5). Besides, late top-to-the-NE

773 narrow localized shear zones, showing a component of brittle deformation, always dip toward  
774 the northeast and are not affected by the doming. We suggest that this doming formed during  
775 regional extension near the brittle-ductile transition by a horizontal-axis rotation beneath the  
776 ETSZ where deformation progressively localized. The Tenda massif then record a re-  
777 localization of strain during its second crossing through the brittle-ductile transition zone,  
778 from strongly distributed at depth where exhumation began, to strongly localized in the upper  
779 levels of the crust, toward the brittle field (Fig. 12).

780

### 781 6.3. Internal factors for strain distribution during burial and exhumation

782

783 The two major shear zones of the Tenda massif are the ETSZ and the SSZ, where  
784 strain localizes toward lithological contacts between rocks of very contrasting rheology (Fig.  
785 10). The fact that strain localizes in the ETSZ is comprehensible since the contact between the  
786 Tenda massif and the Schistes Lustrés nappe is both a zone of lithological/rheological contrast  
787 and a pathway for fluids (Maggi et al., 2012). In agreement with these authors, we find very  
788 heterogeneous second-order strain gradients in the ETSZ (see punctual observations of strain  
789 grades in Fig. 10). Maggi et al. (2012) explain it by alternating episodes of fluids-induced  
790 strain softening (feldspar-to-micas reaction) and strain hardening (neo-blastesis of K-feldspar)  
791 producing a rheological contrast that drives strain localization through a heterogeneous shear  
792 zone. But the internal lithological contacts are also preferentially used for strain localization.  
793 Indeed, most of those contacts are intensely deformed. This is true at the contact between: i)  
794 the granitic complex and the volcano-sedimentary sequence in the Punta di Mignola (Fig. 5g),  
795 ii) the Mt Genova and the Saleccia rhyolite in the SSZ (Figs. 5b and 10), or iii) the Mt Genova  
796 and the Casta granodiorite, east of Mt Genova (Fig. 10). This is in agreement with studies  
797 showing that shear zones nucleate on rheological heterogeneities such as brittle structures

798 (e.g. Mancktelow and Pennacchioni, 2005; Goncalves et al., 2012; 2016; Sullivan et al., 2013)  
799 or lithological contacts (e.g. Pennacchioni and Mancktelow, 2007; Rennie et al., 2013) where  
800 strain remained localized.

801  $S_2$  crenulation is well developed in these preferential zones for strain localization,  
802 particularly in the vicinity of the SSZ and the ETSZ, where  $S_2$  fabrics are visible at landscape  
803 scales (Figs. 3f and 3g). Inversely, in less deformed zone,  $D_2$  folds are rather characterized by  
804  $S_1$  undulations without crenulation development (Fig. 3a). The fact that top-to-the-SW shear  
805 bands are privileged structures where  $S_2$  develops (see section 5 about strain grades) suggests  
806 that penetrative  $S_2$  fabrics visible in the major shear zones of the ETSZ are domain where top-  
807 to-the-SW  $D_1$  shear zones initially localized during burial. Lithological contact thus is a  
808 primordial factor driving strain localization, directly for burial and  $D_1$  structures, and  
809 indirectly for exhumation and  $D_2$  structures, through a structural control of primarily  
810 deformation zone born during  $D_1$ .

811 If lithological contact is a driving structure for strain localization, accommodation of  
812 deformation largely varies in function of the protolith. The best example is the Casta  
813 granodiorite that remained globally undeformed as it resisted in a large scale strain shadow.  
814 The Mt Genova also remained relatively poorly deformed with only few narrow shear zones  
815 situated structurally below and above. Inversely, deformation pervasively and intensely  
816 affected the Saleccia rhyolite and the Mt Asto monzogranite. Maggi et al. (2012; 2014)  
817 described the Casta granodiorite as the protolith of the ETSZ. However, we rather prefer the  
818 geological outline of Rossi et al. (1994) that shows that the ETSZ developed in the Mt Asto  
819 monzogranite. Indeed, when poorly deformed, it is clear that the ETSZ developed in a  
820 relatively felsic facies (Fig. 6a) compared to the Casta granodiorite that is more basic and  
821 characterized by a higher amount of hornblendes (Fig. 7a). Except for the Saleccia rhyolite  
822 that can deform easily due to its rather fine-grained matrix, the fact that plutonic granitoids

823 behaved differently during deformation suggests that deformation mechanisms depend on the  
824 composition of the protolith (X) as an internal parameter together with external parameters  
825 such as fluids, *P-T* conditions, associated with mineral transformations, as suggested for the  
826 Tenda massif (Gueydan et al., 2003; Maggi et al., 2014) or other granites-related shear zone  
827 (e.g. Goncalves et al., 2012; 2016; Oliot et al., 2010; 2014).

828

## 829 7. Conclusion

830

831 This structural study is based on a large dataset collected over most of the Tenda  
832 massif, providing new insights into its history from burial ( $D_1$ ) to exhumation ( $D_2$ ):

833 - The first order finite structure of the Tenda massif is characterized by a NW-SE  
834 dome of  $D_2$  related structures ( $D_2$  folds,  $L_2$ ,  $S_2$  and top-to-the-NE shear criteria) mantling a  
835 less deformed core where  $D_1$  structures ( $L_1$ ,  $S_1$  and top-to-the-SW shear criteria) remain  
836 preserved in their initial position.

837 - Field evidence demonstrates that both  $D_1$  and  $D_2$  structures affect the whole massif.  
838 Although  $D_1$  structures can still be encountered in their initial position, they are generally  
839 reworked by  $D_2$  deformation.

840 - Burial occurred from surface, where localized deformation was concentrated along  
841 thrusts at the top of continental material (visible further south in Corte slices), until blueschist-  
842 facies conditions where deformation was rather distributed, affecting both continental and  
843 oceanic material.

844 - Exhumation probably started in a syn-orogenic context or simply at peak-  
845 metamorphic conditions, with delocalization of thrusting from the ETSZ toward the more  
846 external domains.  $D_2$  deformation then occurred firstly distributed through a general folding  
847 of previous structures, even the original thrust between the Tenda massif and the overlying

848 Schistes Lustrés nappe. Through the switch from syn-orogenic to post-orogenic exhumation,  
849  $D_2$  localized in a set of large-scale shear zones including notably the ETSZ, located at the roof  
850 of the dome between continental and oceanic material, and the SSZ, an internal shear zone  
851 described for the first time. The general doming of  $D_2$  structures occurred during this strain  
852 localization. The final increments are localized in the ETSZ and scattered in the rest of the  
853 massif through narrow semi-brittle shear zones, not affected by doming.

854 - Lithological contacts were site of preferred localization, directly for burial and  $D_1$   
855 structures, and indirectly for exhumation and  $D_2$  structures, through a structural control of  
856 primarily deformation zone born during  $D_1$ . The deformation style and the tectonic coupling  
857 between continental and oceanic material seem to have been mostly controlled by external  
858 parameters, notably depth (i.e.  $P$ - $T$  conditions) in the wedge. However, the strain intensity  
859 map shows that the amount of deformation depends at least in part on the protolith nature that  
860 can, through an interaction with  $P$ - $T$ -fluids conditions, have a strong impact on the  
861 deformation style and the rheology of continental material.

862

863 Acknowledgments

864

865 The early stages of this work were conducted together with Christophe Brunet in the  
866 framework of his PhD. Christophe sadly passed away while he was canoeing a river in the  
867 Alps. This paper is dedicated to him.

868 Giancarlo Molli, Emilien Oliot and Federico Rossetti are thanked for their constructive  
869 comments and suggestions that improved the manuscript. This work has received funding  
870 from the European Research Council (ERC) under the seventh Framework Programme of the  
871 European Union (ERC Advanced Grant, grant agreement No 290864, RHEOLITH), from the  
872 Institut Universitaire de France and from the Labex VOLTAIRE.

873

874 References

875

876 Agard, P. & Vitale-Brovarone, A. (2013). Thermal regime of continental subduction: The  
877 record from exhumed HP-LT terranes (New Caledonia, Oman, Corsica). *Tectonophysics* 601,  
878 206–215.

879

880 Beccaluva, L., Ohnenstetter, D. & Ohnenstetter, M. (1981). K-Ar age determination on some  
881 Tethyan ophiolites. *Rendiconti della Societa Italiana di Mineralogia e Petrologia* 37, 869–880.

882

883 Bellahsen, N., Jolivet, L., Lacombe, O., Bellanger, M., Boutoux, A., Garcia, S., Mouthereau,  
884 F., Le Pourhiet, L. & Gumiaux, C. (2012). Mechanisms of margin inversion in the external  
885 Western Alps: Implications for crustal rheology. *Tectonophysics* 560–561, 62–83.

886

887 Bellanger, M., Bellahsen, N., Jolivet, L., Baudin, T., Augier, R. & Boutoux, A. (2014).  
888 Basement shear zones development and shortening kinematics in the Ecrins Massif, Western  
889 Alps. *Tectonics* 33, 84–111.

890

891 Bézert, P. & Caby, R. (1988). Sur l'âge post-bartonien des événements tectono-  
892 métamorphiques alpins en bordure orientale de la Corse cristalline (Nord de Corte). *Bulletin*  
893 *de la Societe Geologique de France* 4, 965–971.

894

895 Bonnal, M., Parsy, A., Priou-Lacazedieu, A. & Durand-Delga, M. (1973). Sur la structure de  
896 la Balagne sédimentaire (Corse). *Comptes Rendus de l'Academie des Sciences de Paris* 276,  
897 1949–1952.

- 898
- 899 Borradaile, G. J. & Jackson, M. (2010). Structural geology, petrofabrics and magnetic fabrics  
900 (AMS, AARM, AIRM). *Journal of Structural Geology* 32, 1519–1551.
- 901
- 902 Brunet, C., Monié, P., Jolivet, L. & Cadet, J. P. (2000). Migration of compression and  
903 extension in the Tyrrhenian Sea, insights from Ar-40/Ar-39 ages on micas along a transect  
904 from Corsica to Tuscany. *Tectonophysics* 321, 127–155.
- 905
- 906 Caron, J. M. (1994). Metamorphism and deformation in Alpine Corsica. *Schweizerische*  
907 *Mineralogische Und Petrographische Mitteilungen* 74, 105–114.
- 908
- 909 Caron, J. M., Kienast, J. R. & Triboulet, C. (1981). High-pressure-low-temperature  
910 metamorphism and polyphase alpine deformation at Sant'Andrea di Cotone (eastern Corsica,  
911 France). *Tectonophysics* 78, 419–451.
- 912
- 913 Caron, J. M. & Péquignot, G. (1986). The transition between blue-schist and lawsonite  
914 bearing eclogites on the example of corsican metabasalt. *Lithos* 19, 205–218.
- 915
- 916 Cavazza, W., DeCelles, P. G., Fellin, M. G. & Paganellin, L. (2007). The Miocene Saint-  
917 Florent Basin in northern Corsica: stratigraphy, sedimentology, and tectonic implications.  
918 *Basin Research* 19, 507–527.
- 919
- 920 Charles, N., Gumiaux, C., Augier, R., Chen, Y., Zhu, R. & Lin, W. (2011). Metamorphic  
921 Core Complexes vs. synkinematic plutons in continental extension setting: Insights from key  
922 structures (Shandong Province, eastern China). *Journal of Asian Earth Sciences* 40, 261–278.

923

924 Chemenda, A. I., Mattauer, M., Malavieille, J. & Bokun, A. N. (1995). A mechanism for syn-  
925 collisional rock exhumation and associated normal faulting: Results from physical modelling.  
926 *Earth and Planetary Science Letters* 132, 225–232.

927

928 Cohen, C. R., Schweickert, R. A. & Odom, A. L. (1981). Age of emplacement of the schistes  
929 Lustrés nappe, Alpine Corsica. *Tectonophysics* 73, 267–283.

930

931 Daniel, J. M., Jolivet, L., Goffé, B. & Poinssot, C. (1996). Crustal-scale strain partitioning:  
932 footwall deformation below the Alpine Oligo-Miocene detachment of Corsica. *Journal of*  
933 *Structural Geology* 18, 41–59.

934

935 De Wever, P., Danelian, T., Durand-Delga, M., Cordey, F. & Kito, N. (1987). Datations des  
936 radiolarites post-ophiolitiques de Corse alpine à l'aide des radiolaires. *Comptes Rendus de*  
937 *l'Academie des Sciences de Paris* 305, 893–900.

938

939 Di Rosa, M., De Giorgi, A., Marroni, M. & Vidal, O. (2016). Syn-convergence exhumation of  
940 continental crust: evidence from structural and metamorphic analysis of the Monte Cecu area,  
941 Alpine Corsica (Northern Corsica, France). *Geological Journal*.

942

943 Di Vincenzo, G., Grande, A., Prosser, G., Cavazza, W. & DeCelles, P. G. (2016).  $^{40}\text{Ar}$ – $^{39}\text{Ar}$   
944 laser dating of ductile shear zones from central Corsica (France): Evidence of Alpine (middle  
945 to late Eocene) syn-burial shearing in Variscan granitoids. *Lithos* 262, 369–383.

946

- 947 Doglioni, C. (1991). A proposal for the kinematic modelling of W-dipping subductions -  
948 possible applications to the Tyrrhenian-Apennines system. *Terra Nova* 3, 423–434.  
949
- 950 Durand-Delga, M. (1984). Principaux traits de la Corse Alpine et corrélations avec les Alpes  
951 Ligure. *Memorie della Societa Geologica Italiana* 28, 285–329.  
952
- 953 Egal, E. & Caron, J. M. (1989). Structures de l'Eocène autochtone en Corse. *Comptes Rendus*  
954 *de l'Academie des Sciences de Paris* 309, 1431–1436.  
955
- 956 Faccenna, C., Piromallo, C., Crespo-Blanc, A., Jolivet, L. & Rossetti, F. (2004). Lateral slab  
957 deformation and the origin of the western Mediterranean arcs. *Tectonics* 23, TC1012.  
958
- 959 Faccenna, C., Speranza, F., D'Ajello Caracciolo, F., Mattei, M. & Giacomo, O. (2002).  
960 Extensional tectonics on Sardinia (Italy): insights into the arc–back-arc transitional regime.  
961 *Tectonophysics* 356, 213–232.  
962
- 963 Faure, M. & Malavieille, J. (1980). Les plis en fourreau du substratum de la Nappe des  
964 Schistes Lustrés de Corse. Signification cinématique. *Comptes Rendus de l'Academie des*  
965 *Sciences de Paris* 290, 1349–1352.  
966
- 967 Faure, M. & Malavieille, J. (1981). Etude structurale d'un cisaillement ductile □: le charriage  
968 ophiolitique corse dans la région de Bastia. *Bulletin de la Societe Geologique de France* 23,  
969 335–345.  
970

- 971 Fellin, M. G., Vance, J. A., Garver, J. I. & Zattin, M. (2006). The thermal evolution of  
972 Corsica as recorded by zircon fission-tracks. *Tectonophysics* 421, 299–317.  
973
- 974 Ferrandini, J., Gattacceca, J., Ferrandini, M., Deino, A. & Janin, M.-C. (2003).  
975 Chronostratigraphie et paléomagnétisme des dépôts oligo-miocènes de Corse: implications  
976 géodynamiques pour l'ouverture du bassin liguro-provençal. *Bulletin de la Societe  
977 Geologique de France* 174, 357–371.  
978
- 979 Ferrandini, M., Ferrandini, J., Loÿe-Pilot, M.-D., Butterlin, J., Cravatte, J. & Janin, M.-C.  
980 (1998). Le Miocène du bassin de Saint-Florent (Corse): Modalités de la transgression du  
981 Burdigalien supérieur et mise en évidence du Serravallien. *Geobios* 31, 125–137.  
982
- 983 Fournier, M., Jolivet, L., Goffé, B. & Dubois, R. (1991). Alpine Corsica Metamorphic Core  
984 Complex. *Tectonics* 10, 1173–1186.  
985
- 986 Garfagnoli, F., Menna, F., Pandeli, E. & Principi, G. (2009). Alpine metamorphic and tectonic  
987 evolution of the Inzecca-Ghisoni area (southern Alpine Corsica, France). *Geological Journal*  
988 44, 191–210.  
989
- 990 Gibbons, W. & Horak, J. (1984). Alpine metamorphism of Hercynian hornblende granodiorite  
991 beneath the blueschist facies schistes-lustrés nappe of NE Corsica. *Journal of Metamorphic  
992 Geology* 2, 95–113.  
993

- 994 Goncalves, P., Olliot, E., Marquer, D. & Connolly, J. A. D. (2012). Role of chemical processes  
995 on shear zone formation: an example from the Grimsel metagranodiorite (Aar massif, Central  
996 Alps). *Journal of Metamorphic Geology* 30.
- 997
- 998 Goncalves, P., Poilvet, J.-C., Olliot, E., Trap, P. & Marquer, D. (2016). How does shear zone  
999 nucleate? An example from the Suretta nappe (Swiss Eastern Alps). *Journal of Structural*  
1000 *Geology* 86, 166–180.
- 1001
- 1002 Gueguen, E., Doglioni, C. & Fernandez, M. (1998). On the post-25 Ma geodynamic evolution  
1003 of the western Mediterranean. *Tectonophysics* 298, 259–269.
- 1004
- 1005 Gueydan, F., Leroy, Y. M., Jolivet, L. & Agard, P. (2003). Analysis of continental midcrustal  
1006 strain localization induced by microfracturing and reaction-softening. *Journal of Geophysical*  
1007 *Research* 108, 2064.
- 1008
- 1009 Huet, B., Labrousse, L. & Jolivet, L. (2009). Thrust or detachment? Exhumation processes in  
1010 the Aegean: Insight from a field study on Ios (Cyclades, Greece). *Tectonics* 28, TC3007.
- 1011
- 1012 Ingles, J., Lamouroux, C., Soula, J.-C., Guerrero, N. & Debat, P. (1999). Nucleation of ductile  
1013 shear zones in a granodiorite under greenschist facies conditions, Néouvielle massif,  
1014 Pyrenees, France. *Journal of Structural Geology* 21, 555–576.
- 1015
- 1016 Jakni, B., Poupeau, G., Sosson, M., Rossi, P., Ferrandini, J. & Guennoc, P. (2000).  
1017 Dénudations cénozoïques en Corse: une analyse thermochronologique par traces de fission  
1018 sur apatites. *Comptes Rendus de l'Academie des Sciences de Paris* 331, 775–782.

- 1019
- 1020 Jolivet, L. et al. (1998). Midcrustal shear zones in postorogenic extension: Example from the  
1021 northern Tyrrhenian Sea. *Journal of Geophysical Research* 103, 12123–12160.
- 1022
- 1023 Jolivet, L., Augier, R., Faccenna, C., Negro, F., Rimmelé, G., Agard, P., Robin, C., Rossetti,  
1024 F. & Crespo-Blanc, A. (2008). Subduction, convergence and the mode of backarc extension in  
1025 the Mediterranean region. *Bulletin de la Societe Geologique de France* 179, 525–550.
- 1026
- 1027 Jolivet, L., Daniel, J. M. & Fournier, M. (1991). Geometry and kinematics of extension in  
1028 Alpine Corsica. *Earth and Planetary Science Letters* 104, 278–291.
- 1029
- 1030 Jolivet, L., Dubois, R., Fournier, M., Goffé, B., Michard, A. & Jourdan, C. (1990). Ductile  
1031 extension in alpine Corsica. *Geology* 18, 1007–1010.
- 1032
- 1033 Jolivet, L., Gorini, C., Smit, J. & Leroy, S. (2015). Continental breakup and the dynamics of  
1034 rifting in back-arc basins: The Gulf of Lion margin. *Tectonics* 34, 662–679.
- 1035
- 1036 Jourdan, C. (1988). *Balagne orientale et massif du Tenda (Corse septentrionale): étude*  
1037 *structurale, interprétation des accidents et des déformations, reconstitutions géodynamiques.*  
1038 *Thèse de Doctorat, Orsay, Université de Paris-Sud.*
- 1039
- 1040 Lacombe, O. & Jolivet, L. (2005). Structural and kinematic relationships between Corsica and  
1041 the Pyrenees-Provence domain at the time of the Pyrenean orogeny. *Tectonics* 24, TC1003.
- 1042

- 1043 Lahondère, D. (1988). Le métamorphisme éclogitique dans les orthogneiss et les metabasites  
1044 ophiolitiques de la région de Farinole (Corse). Bulletin de la Societe Geologique de France 4,  
1045 579–585.
- 1046
- 1047 Lahondère, D. & Guerrot, C. (1997). Datation Sm-Nd du métamorphisme éclogitique en  
1048 Corse alpine: un argument pour l'existence au Crétacé supérieur d'une zone de subduction  
1049 active localisée sous le bloc corso-sarde. Géologie de la France 3, 3–11.
- 1050
- 1051 Launeau, P. & Robin, P.-Y. F. (2005). Determination of fabric and strain ellipsoids from  
1052 measured sectional ellipses—implementation and applications. Journal of Structural Geology  
1053 27, 2223–2233.
- 1054
- 1055 Laurent, V., Beaudoin, A., Jolivet, L., Arbaret, L., Augier, R., Rabillard, A. & Menant, A.  
1056 (2015). Interrelations between extensional shear zones and synkinematic intrusions: The  
1057 example of Ikaria Island (NE Cyclades, Greece). Tectonophysics 651–652, 152–171.
- 1058
- 1059 Leloup, P. H., Arnaud, N., Sobel, E. R. & Lacassin, R. (2005). Alpine thermal and structural  
1060 evolution of the highest external crystalline massif: The Mont Blanc. Tectonics 24, TC4002.
- 1061
- 1062 Maffione, M., Speranza, F., Faccenna, C., Cascella, A., Vignaroli, G. & Sagnotti, L. (2008). A  
1063 synchronous Alpine and Corsica-Sardinia rotation. Journal of Geophysical Research 113,  
1064 B03104.
- 1065
- 1066 Maggi, M., Rossetti, F., Corfu, F., Theye, T., Andersen, T. B. & Faccenna, C. (2012).  
1067 Clinopyroxene-rutile phyllonites from the East Tenda Shear Zone (Alpine Corsica, France):

1068 pressure-temperature-time constraints to the Alpine reworking of Variscan Corsica. *Journal of*  
1069 *the Geological Society* 169, 723–732.

1070

1071 Maggi, M., Rossetti, F., Ranalli, G. & Theye, T. (2014). Feedback between fluid infiltration  
1072 and rheology along a regional ductile-to-brittle shear zone: The East Tenda Shear Zone  
1073 (Alpine Corsica). *Tectonics* 33, 253–280.

1074

1075 Malasoma, A. & Marroni, M. (2007). HP/LT metamorphism in the Volparone Breccia  
1076 (Northern Corsica, France): evidence for involvement of the Europe/Corsica continental  
1077 margin in the Alpine subduction zone. *Journal of Metamorphic Geology* 25, 529–545.

1078

1079 Malasoma, A., Marroni, M., Musumeci, G. & Pandolfi, L. (2006). High-pressure mineral  
1080 assemblage in granitic rocks from continental units, Alpine Corsica, France. *Geological*  
1081 *Journal* 41, 49–59.

1082

1083 Malavieille, J., Chemenda, A. & Larroque, C. (1998). Evolutionary model for Alpine Corsica:  
1084 mechanism for ophiolite emplacement and exhumation of high-pressure rocks. *Terra Nova* 10,  
1085 317–322.

1086

1087 Malinverno, A. & Ryan, W. B. F. (1986). Extension in the Tyrrhenian Sea and shortening in  
1088 the Apennines as result of arc migration driven by sinking of the lithosphere. *Tectonics* 5,  
1089 227–245.

1090

1091 Malusà, M. G. et al. (2015). Contrasting styles of (U)HP rock exhumation along the Cenozoic  
1092 Adria-Europe plate boundary (Western Alps, Calabria, Corsica). *Geochemistry Geophysics*  
1093 *Geosystems* 16, 1786–7824.

1094

1095 Maluski, H. (1977). Application de la méthode  $^{40}\text{Ar}/^{39}\text{Ar}$  aux minéraux des roches  
1096 cristallines perturbées par les événements thermiques et tectoniques en Corse. *Bulletin de la*  
1097 *Societe Geologique de France* 19, 849–855.

1098

1099 Mancktelow, N. S. & Pennacchioni, G. (2005). The control of precursor brittle fracture and  
1100 fluid-rock interaction on the development of single and paired ductile shear zones. *Journal of*  
1101 *Structural Geology* 27, 645–661.

1102

1103 Martin, L. A. J., Rubatto, D., Brovarone, A. V. & Hermann, J. (2011). Late Eocene lawsonite-  
1104 eclogite facies metasomatism of a granulite sliver associated to ophiolites in Alpine Corsica.  
1105 *Lithos* 125, 620–640.

1106

1107 Mattauer, M., Faure, M. & Malavieille, J. (1981). Transverse lineation and large-scale  
1108 structures related to Alpine obduction in Corsica. *Journal of Structural Geology* 3, 401–409.

1109

1110 Meresse, F., Lagabrielle, Y., Malavieille, J. & Ildefonse, B. (2012). A fossil Ocean–Continent  
1111 Transition of the Mesozoic Tethys preserved in the Schistes Lustrés nappe of northern  
1112 Corsica. *Tectonophysics* 579, 4–16.

1113

- 1114 Molli, G. (2008). Northern Apennine-Corsica orogenic system: an updated overview. In:  
1115 Siegesmund, S., Fügenschuh, B., Froitzheim, N. (Eds.), Tectonic Aspects of the Alpine-  
1116 Dinaride-Carpathian System. Geological Society, London, Special Publications 298, 413–442.  
1117
- 1118 Molli, G. & Malavieille, J. (2011). Orogenic processes and the Corsica/Apennines  
1119 geodynamic evolution: insights from Taiwan. *International Journal of Earth Sciences* 100,  
1120 1207–1224.  
1121
- 1122 Molli, G. & Tribuzio, R. (2004). Shear zones and metamorphic signature of subducted  
1123 continental crust as tracers of the evolution of the Corsica/Northern Apennine orogenic  
1124 system. Geological Society, London, Special Publications 224, 321–335.  
1125
- 1126 Molli, G., Tribuzio, R. & Marquer, D. (2006). Deformation and metamorphism at the eastern  
1127 border of the Tenda Massif (NE Corsica): a record of subduction and exhumation of  
1128 continental crust. *Journal of Structural Geology* 28, 1748–1766.  
1129
- 1130 Mouthereau, F., Tensi, J., Bellahsen, N., Lacombe, O., De Boisgrollier, T. & Kargar, S.  
1131 (2007). Tertiary sequence of deformation in a thin-skinned/thick-skinned collision belt: The  
1132 Zagros Folded Belt (Fars, Iran). *Tectonics* 26, TC5006.  
1133
- 1134 Mouthereau, F., Watts, A. B. & Burov, E. (2013). Structure of orogenic belts controlled by  
1135 lithosphere age. *Nature Geoscience* 6, 785–789.  
1136

- 1137 Ohnenstetter, M., Ohnenstetter, D., Vidal, P., Cornichet, J., Hermitte, D. & Mace, J. (1981).  
1138 Crystallization and age of zircon from Corsican ophiolitic albitites: consequences for oceanic  
1139 expansion in Jurassic times. *Earth and Planetary Science Letters* 54, 397–408.
- 1140
- 1141 Olliot, E., Goncalves, P. & Marquer, D. (2010). Role of plagioclase and reaction softening in a  
1142 metagranite shear zone at mid-crustal conditions (Gotthard Massif, Swiss Central Alps).  
1143 *Journal of Metamorphic Geology* 28, 849–871.
- 1144
- 1145 Olliot, E., Goncalves, P., Schulmann, K., Marquer, D. & Lexa, O. (2014). Mid-crustal shear  
1146 zone formation in granitic rocks: Constraints from quantitative textural and crystallographic  
1147 preferred orientations analyses. *Tectonophysics* 612–613, 63–80.
- 1148
- 1149 Oudet, J., Münch, P., Borgomano, J., Quillevère, F., Melinte-Dobrinescu, M. C., Demory, F.,  
1150 Viseur, S. & Cornee, J.-J. (2010). Land and sea study of the northeastern golfe du Lion rifted  
1151 margin: the Oligocene–Miocene of southern Provence (Nerthe area, SE France). *Bulletin de la*  
1152 *Société géologique de France* 181, 591–607.
- 1153
- 1154 Pennacchioni, G. & Mancktelow, N. S. (2007). Nucleation and initial growth of a shear zone  
1155 network within compositionally and structurally heterogeneous granitoids under amphibolite  
1156 facies conditions. *Journal of Structural Geology* 29, 1757–1780.
- 1157
- 1158 Raimbourg, H., Jolivet, L., Labrousse, L., Leroy, Y. & Avigad, D. (2005). Kinematics of  
1159 syneclogite deformation in the Bergen Arcs, Norway: implications for exhumation  
1160 mechanisms. In: Gapais, D., Brun, J. P., Cobbold, P. R. (Eds.), *Deformation Mechanisms,*

- 1161 Rheology and Tectonics: from Minerals to the Lithosphere. Geological Society, London,  
1162 Special Publications 243, 175–192.
- 1163
- 1164 Ravna, E. J. K., Andersen, T. B., Jolivet, L. & De Capitani, C. (2010). Cold subduction and  
1165 the formation of lawsonite eclogite – constraints from prograde evolution of eclogitized  
1166 pillow lava from Corsica. *Journal of Metamorphic Geology* 28, 381–395.
- 1167
- 1168 Rehault, J.-P., Boillot, G. & Mauffret, A. (1984). The Western Mediterranean Basin  
1169 geological evolution. *Marine Geology* 55, 447–477.
- 1170
- 1171 Rennie, S. F., Fagereng, A. & Diener, J. F. A. (2013). Strain distribution within a km-scale,  
1172 mid-crustal shear zone: The Kuckaus Mylonite Zone, Namibia. *Journal of Structural Geology*  
1173 56, 57–69.
- 1174
- 1175 Rossetti, F., Faccenna, C., Goffé, B., Monié, P., Argentieri, A., Funicello, R. & Mattei, M.  
1176 (2001). Alpine structural and metamorphic signature of the Sila Piccola Massif nappe stack  
1177 (Calabria, Italy): Insights for the tectonic evolution of the Calabrian Arc. *Tectonics* 20, 112–  
1178 133.
- 1179
- 1180 Rossetti, F., Glodny, J., Theye, T. & Maggi, M. (2015). Pressure-temperature-deformation-  
1181 time of the ductile Alpine shearing in Corsica: From orogenic construction to collapse. *Lithos*  
1182 218–219, 99–116.
- 1183
- 1184 Rossi, P. et al. (2001). Carte Géologique de France (1/50 000), feuille de Santo-Pietro-Di-  
1185 Tenda (1106). Bureau des Recherches Géologiques et Minières.

- 1186
- 1187 Rossi, P., Durand-Delga, M. & Cocherie, A. (1993). Caractère volcano-plutonique du  
1188 magmatisme calco-alcalin composite d'âge Stéphanien supérieur-Permien inférieur en Corse.  
1189 Comptes Rendus de l'Académie des Sciences de Paris 316, 1779–1788.
- 1190
- 1191 Rossi, P., Lahondère, J.-C., Lluch, D., Loÿe-Pilot, M.-D. & Jacquet, M. (1994). Carte  
1192 Géologique de France (1/50 000), feuille de Saint-Florent (1103). Bureau des Recherches  
1193 Géologiques et Minières.
- 1194
- 1195 Séranne, M. (1999). The Gulf of Lion continental margin (NW Mediterranean) revisited by  
1196 IBS: an overview. In: Durand, B., Jolivet, L., Horvath, F., Séranne, M. (Eds.), Tertiary  
1197 Extension within the Alpine Orogen. Geological Society, London, Special Publications 156,  
1198 15–36.
- 1199
- 1200 Speranza, F., Villa, I. M., Sagnotti, L., Florindo, F., Cosentino, D., Cipollari, P. & Mattei, M.  
1201 (2002). Age of the Corsica–Sardinia rotation and Liguro–Provençal Basin spreading: new  
1202 paleomagnetic and Ar/Ar evidence. *Tectonophysics* 347, 231–251.
- 1203
- 1204 Sullivan, W. A., Boyd, A. S. & Monz, M. E. (2013). Strain localization in homogeneous  
1205 granite near the brittle–ductile transition: A case study of the Kellyland fault zone, Maine,  
1206 USA. *Journal of Structural Geology* 56, 70–88.
- 1207
- 1208 Tribuzio, R. & Giacomini, F. (2002). Blueschist facies metamorphism of peralkaline rhyolites  
1209 from the Tenda crystalline massif (northern Corsica): evidence for involvement in the Alpine  
1210 subduction event? *Journal of Metamorphic Geology* 20, 513–526.

- 1211
- 1212 Vitale Brovarone, A., Beltrando, M., Malavieille, J., Giuntoli, F., Tondella, E., Groppo, C.,  
1213 Beyssac, O. & Compagnoni, R. (2011a). Inherited Ocean-Continent Transition zones in  
1214 deeply subducted terranes: Insights from Alpine Corsica. *Lithos* 124, 273–290.
- 1215
- 1216 Vitale Brovarone, A., Beyssac, O., Malavieille, J., Molli, G., Beltrando, M. & Compagnoni,  
1217 R. (2013). Stacking and metamorphism of continuous segments of subducted lithosphere in a  
1218 high-pressure wedge: The example of Alpine Corsica (France). *Earth-Science Reviews* 116,  
1219 35–56.
- 1220
- 1221 Vitale Brovarone, A., Groppo, C., Hetényi, G., Compagnoni, R. & Malavieille, J. (2011b).  
1222 Coexistence of lawsonite-bearing eclogite and blueschist: phase equilibria modelling of  
1223 Alpine Corsica metabasalts and petrological evolution of subducting slabs. *Journal of*  
1224 *Metamorphic Geology* 29, 583–600.
- 1225
- 1226 Vitale Brovarone, A. V. & Herwartz, D. (2013). Timing of HP metamorphism in the Schistes  
1227 Lustres of Alpine Corsica: New Lu-Hf garnet and lawsonite ages. *Lithos* 172, 175–191.
- 1228
- 1229 Zarki-Jakni, B., van der Beek, P., Poupeau, G., Sosson, M., Labrin, E., Rossi, P. & Ferrandini,  
1230 J. (2004). Cenozoic denudation of Corsica in response to Ligurian and Tyrrhenian extension:  
1231 Results from apatite fission track thermochronology. *Tectonics* 23, TC1003.
- 1232
- 1233 Figures Captions
- 1234

1235 Figure 1. Geological map of the studied area. (a) Tectonic map of western Mediterranean  
1236 region. (b) Geological map of Alpine Corsica associated with a representative cross-section  
1237 (modified after Vitale Brovarone et al., 2013). Ce: Centuri continental unit; Fa: Farinole  
1238 continental unit; In: Inzecca unit; Ma: Macinaggio unit; Ne: Nebbio unit; Sa: Sampolo unit;  
1239 SDP: Serra di Pigno continental unit; SL: Santa Lucia; Pi: Pineto ophiolitic unit; Po:  
1240 Popolasca unit.

1241  
1242 Figure 2. Simplified geological map (modified after Rossi et al., 1994; 2001) with main planar  
1243 fabrics of the Tenda massif. (a) Foliation map. (b)  $S_2$  trajectories map. Note that  $S_2$  depicts  
1244 anastomosing structures around grey zones that represent volumes where  $S_1$  or even  
1245 undeformed rocks are preserved. (c) Statistics of the foliations geometries. Foliation poles are  
1246 presented with density contours in Schmidt's lower hemisphere equal-area projection and  
1247 strike preferred orientations are given by rose-diagrams. Geometries of the large-scale were  
1248 retrieved by the SW-NE elongation of the clouds showing a NW-SE dome.  $S_1$  and  $S_2$  strikes  
1249 are characterized by different preferred orientations from N170°E to N140°E, respectively.  
1250 Note that the  $S_2$  dip is relatively flat comparing to  $S_1$  that displays more dispersed dips from  
1251 flat to vertical.

1252  
1253 Figure 3. Characterization of the main planar fabrics and folds at different scales. (a)  
1254 Subvertical  $S_1$  of the Mt Genova (view from the south). (b) Close-up view of  $D_2$  folds  
1255 affecting  $S_1$  and associated with the development of a  $S_2$  crenulation cleavage in the center of  
1256 the Tenda massif (N 42.654838° E 9.190533°). (c) Close-up view of  $D_2$  folds and folded  $S_1$   
1257 associated with the development of a  $S_2$  crenulation cleavage in the lowermost structural  
1258 levels of the ETSZ (N 42.640269° E 9.264771°). Note that  $S_1$  carries blue-amphibole formed  
1259 during  $D_1$ . (d) Microscopic view from the previous outcrop (insert c). Note that  $S_1$  carries

1260 blue-amphiboles that are retrogressed into chlorite in  $S_2$  cleavage. (e) Equal-area projection  
1261 plots (Schmidt's lower hemisphere) of structural features characterizing  $D_2$  folds from typical  
1262 outcrops over the Tenda massif: Envelopes of folded  $S_1$  are steeply dipping while  $S_2$  is sub-  
1263 horizontal, both striking NNW-SSE, just as the  $D_2$  fold axis trends.

1264

1265 Figure 3 (continued). (f and g) Landscape views of the Saleccia Shear Zone (SSZ) (f: view  
1266 from the main D81 road) and the ETSZ (g: view from the Punta Mortella) both marked by the  
1267 development of a penetrative  $S_2$  fabric.  $S_2$  planes from the SSZ and the ETSZ are plotted. (h)  
1268 Late  $D_2$  folds affecting  $S_2$  in the Punta Mortella (N 42.718401° E 9.250547°). (i) Equal-area  
1269 projection plots (Schmidt's lower hemisphere) of late  $D_2$  folds axis of the ETSZ from Punta di  
1270 Cepo to Punta Mortella. Note that axis trends evolve from NNW-SSE away from the ETSZ  
1271 (Fig. 3e) to ENE-WSW near its most deformed parts.

1272

1273 Figure 4. Stretching lineations of the Tenda massif. (a) Stretching lineation map and  
1274 associated sense of shear. (b) Statistics of the stretching lineations geometries. Lineation poles  
1275 are presented with density contours in Schmidt's lower hemisphere equal-area projection and  
1276 trends preferred orientations are given by rose-diagrams. Note that  $L_1$  and  $L_2$  trends are  
1277 characterized by slightly different preferred orientations from N063°E to N052°E,  
1278 respectively.

1279

1280 Figure 5. Kinematics of  $D_2$  deformation in the whole Tenda massif. (a) Representative cross  
1281 section of the Tenda massif from west to east showing the large-scale structures and the  
1282 geometries of  $D_2$  top-to-the-NE (green) and  $D_1$  top-to-the-SW shearing (blue). Note that both  
1283  $D_1$  and  $D_2$  affect the whole massif; the undeformed Variscan protolith being locally preserved.  
1284 Also showed are stereographic projections of structures along the cross-section. Letters

1285 highlight the position of pictures presented in the rest of figure 5. (b) Top-to-the-NE  
1286 mylonites in the Saleccia rhyolite, west of Saleccia. (c) Localized top-to-the-NE narrow shear  
1287 zone in the west of the Tenda massif (N 42.667220° E 9.148613°). (d) Localized top-to-the-  
1288 NE steep semi-brittle shear zone affecting an isotropic protolith in the ETSZ (N 42.650459° E  
1289 9.263404°).

1290

1291 Figure 5 (continued). (e) Rhyolite intrusion (top of a small-scale dome) asymmetrically  
1292 boudinaged in a pelitic matrix, west of the Tenda massif (N 42.661448° E 9.130829°). (f)  
1293 Zoom on the previous outcrop: D<sub>2</sub> folds with folded S<sub>1</sub> associated with S<sub>2</sub> crenulation. Note,  
1294 from e and f, that S<sub>2</sub> is sigmoidal in between top-to-the-NE shear bands. (g) Top-to-the-NE  
1295 shearing of a granitic dyke within a micaschists matrix (Punta di Mignola shear zone; contact  
1296 between the volcano-sedimentary sequence and the granitic complex). (h) Blue-amphibole  
1297 forming sigma-clasts compatible with top-to-the-NE shearing in the ETSZ (N 42.658489° E  
1298 9.272518°). (i) Microscopic view in thin section from the previous outcrop. Top-to-the-NE  
1299 shearing is associated with the boudinage and truncation of blue-amphibole that is  
1300 retrogressed into chlorite. Note that crystallization of small blue-amphiboles in tails of sigma-  
1301 clasts also occurs (see white square). (j) Mylonites in the uppermost levels of the ETSZ.  
1302 Mineral association is made of quartz, albite, phengite, chlorite and pyrite (N 42.700461° E  
1303 9.26382°).

1304

1305 Figure 6. Examples of D<sub>1</sub> top-to-the-SW criteria. (a, b, c) Typical outcrop showing preserved  
1306 top-to-the-SW criteria in the lowermost structural levels of the ETSZ (N 42.649840° E  
1307 9.266655°). (a) In poorly deformed zone, gently dipping top-to-the-SW localized shear bands  
1308 affect an undeformed granite. Note that S<sub>1</sub> only develops near shear bands. (b) With  
1309 increasing deformation, the outcrop is characterized by distributed strain with mylonites. Top-

1310 to-the-SW shear bands dip to the west when  $S_1$  appears flat. (c) Top-to-the-SW shearing  
1311 appears sometimes localized through high strain bands. Note that this band widens from the  
1312 left to the right of the picture. Note also that shear bands in (a) and the high strain band in (c)  
1313 have the same orientation. (d) Toward the top of the ETSZ, both  $S_1$  and shear bands dip to the  
1314 east, compatibly with the general trend of the ETSZ (N 42.654916° E 9.267789°). Top-to-the-  
1315 SW shearing is clearly recorded in the blue-amphibole stability field. (e) Cross-cutting  
1316 relationships between top-to-the-NE and top-to-the-SW deformation in the ETSZ (N  
1317 42.656507° E 9.272097°).

1318  
1319 Figure 7.  $D_2$  strain intensity scale in the granitic protolith. (a) Grade 0s.s: outcrop picture of a  
1320 typical isotropic granite (N 42.67536° E 9.22939°). The magmatic parageneses is equant and  
1321 apparently metastable. (b) Grade 0s.s: magmatic hornblendes are incipiently statically  
1322 replaced by blue-amphiboles involved in a coronitic reaction (N 42.66067° E 9.23987°). (c)  
1323 Grade 0W: top-to-the-SW shear bands and sigmoidal  $S_1$  in between (N 42.649840° E  
1324 9.266655°). (d) Grade 1:  $D_2$  folds with crenulated still steeply dipping  $S_1$  and formation of  $S_2$   
1325 crenulation cleavage (N 42.655945° E 9.272113°). Note that deformation is characterized by  
1326 only a pure shear component. (e) Grade 2: appearance of simple shear components on  $S_2$   
1327 cleavage (N 42.700461° E 9.26382°).  $S_1$  in between shows sigmoidal feature indicating top-  
1328 to-the-NE shearing. Angle between shear bands ( $S_2$ ) and foliation ( $S_1$ ) is about 60°. (f)  
1329 Transition between grades 2 and 3: top-to-the-NE shear bands with sigmoidal  $S_2$  in between  
1330 (N 42.70249° E 9.25855°). Spacing between shear bands is around 5-10 cm. Angle between  
1331 shear bands and  $S_2$  is between 60 and 30°.  $D_2$  folds remain visible. (g) Transition between  
1332 grades 3 and 4: penetrative mylonitic fabric (N 42.700461° E 9.26382°). Spacing between  
1333 shear bands is close to 3-2 cm, and angle between shear bands and  $S_2$  is about 30°. (h) Grade

1334 4: development of ultramylonite bodies within strongly flattened mylonitic fabric (N  
1335 42.71928° E 9.23598°). See text for further explanations.

1336

1337 Figure 8. Synoptic view of all strain grades described in figure 7 along a virtual  $D_2$  strain  
1338 gradient. This gradient is characterized by an increase of  $D_2$  fabrics resulting in the  
1339 progressive overprint of  $D_1$  structures. Note that both spacing between shear bands and angle  
1340 between  $S_2$  and top-to-the-NE shear bands decrease upward, from grade 2 to grade 4. Note  
1341 that  $D_1$  fabrics have always been observed at the base of the  $D_2$  strain gradient in close  
1342 association with undeformed rocks.

1343

1344 Figure 9. Examples of structural evidence of the time-sequence relative to the increasing  
1345 strain intensity. Volumes characterized by grade 2 are asymmetrically boudinaged in volumes  
1346 characterized by grade 3 at outcrop (a: N 42.659128° E 9.273212°) and landscape-scales (b: N  
1347 42.71167° E 9.255127°).

1348

1349 Figure 10. Strain grades map of the Tenda massif within granitic protoliths. One of the five  
1350 grades (see Figs. 7 and 8) has been attributed for each of the 617 visited outcrops.  
1351 Interpolation highlights either the overall increase of finite deformation toward the ETSZ and  
1352 the SSZ or more local strain localization. (b) Cross-sections normal to the regional foliation  
1353 and parallel to the regional stretching across the main gradients of deformation. SSZ: Saleccia  
1354 Shear zone; ETSZ: East Tenda Shear Zone.

1355

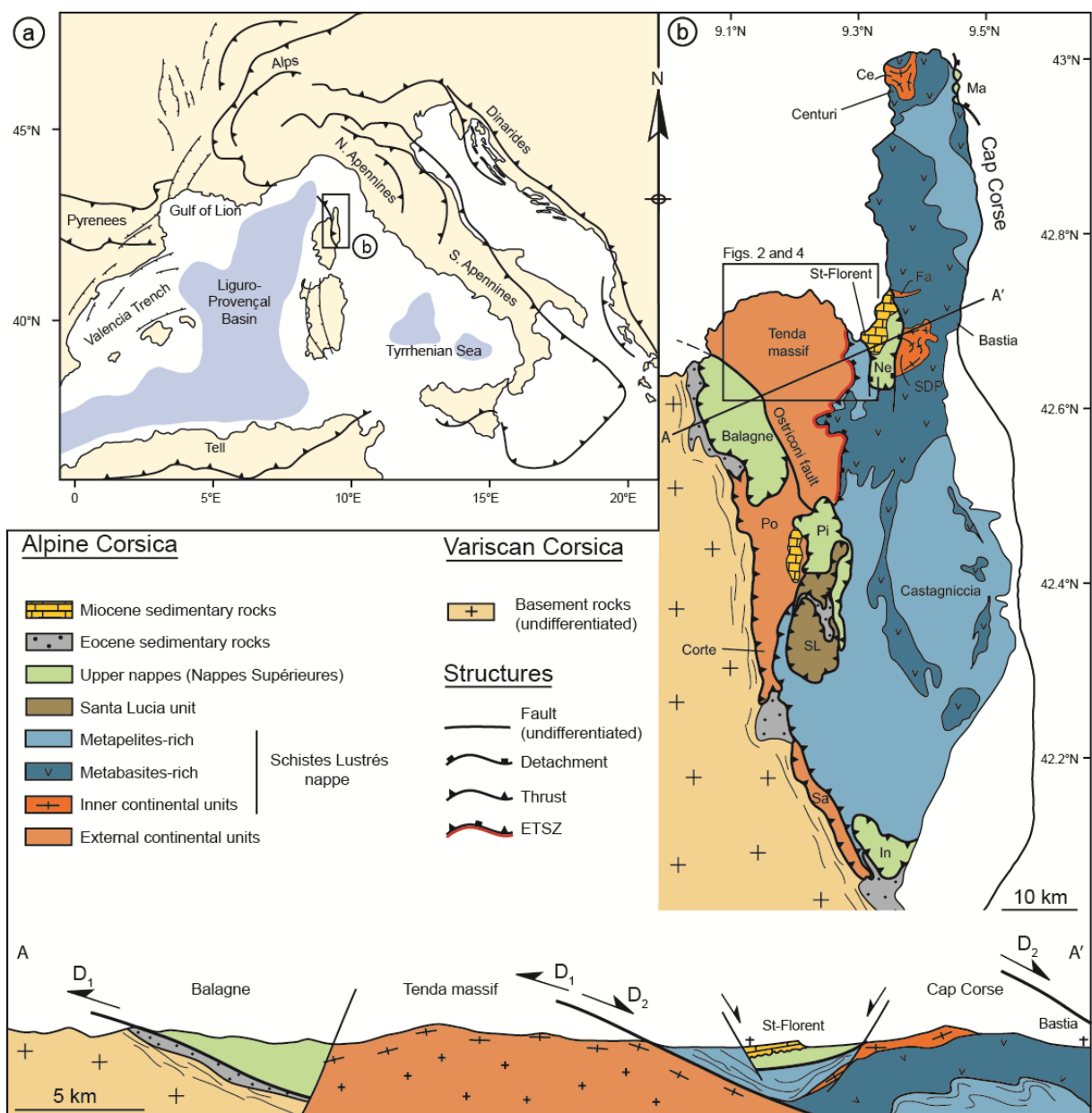
1356 Figure 11. Available biostratigraphic and radiochronologic age constraints of Alpine events  
1357 for the Gulf of Lion basin and Corsica-Sardinia continental portions. Data are from (1)  
1358 Séranne, 1999; Oudet et al., 2010; Jolivet et al., 2015; (2) Faccenna et al., 2002; (3) Speranza

1359 et al., 2002; (4) Bonnal et al., 1973; Bezert and Caby, 1988; Jourdan, 1988; Egal and Caron,  
1360 1989; (5) Ferrandini et al., 2003; (6) Cavazza et al., 2007; (7) Brunet et al., 2000; (8) Martin  
1361 et al., 2011; (9) Vitale Brovarone and Herwartz, 2013; (10) Rossetti et al., 2015; (11) Fellin et  
1362 al., 2006; (12) Jakni et al., 2000; Zarkni-Jakni et al., 2004; (13) Lahondère and Guerrot, 1997;  
1363 (14) Maggi et al., 2012; (15) Di Vincenzo et al., 2016.

1364

1365 Figure 12. Tectonic model of Alpine Corsica orogenic system from Eocene to Miocene  
1366 (inspired from Ravna et al., 2010; Molli and Malavieille, 2011; Vitale Brovarone et al., 2013  
1367 and references on chronological constraints presented in Fig. 11) showing the evolution of  
1368 deformation in the Tenda massif from burial to exhumation. During Late Eocene, the Tenda  
1369 massif was buried underneath the Ligurian accretionary complex until its juxtaposition below  
1370 the Schistes Lustrés nappe, and affected by top-to-the-SW deformation ( $D_1$ ) firstly localized  
1371 then pervasive at maximal depth. There, the two units are tectonically coupled (see also Molli  
1372 et al., 2006). From Middle Oligocene to Miocene, syn-to post-orogenic exhumation was  
1373 marked by a progressive localization of strain from distributed (pervasive  $D_2$  folding of  
1374 previous structures) to localized notably near the ETSZ. All sketches are oriented SW-NE.

1375

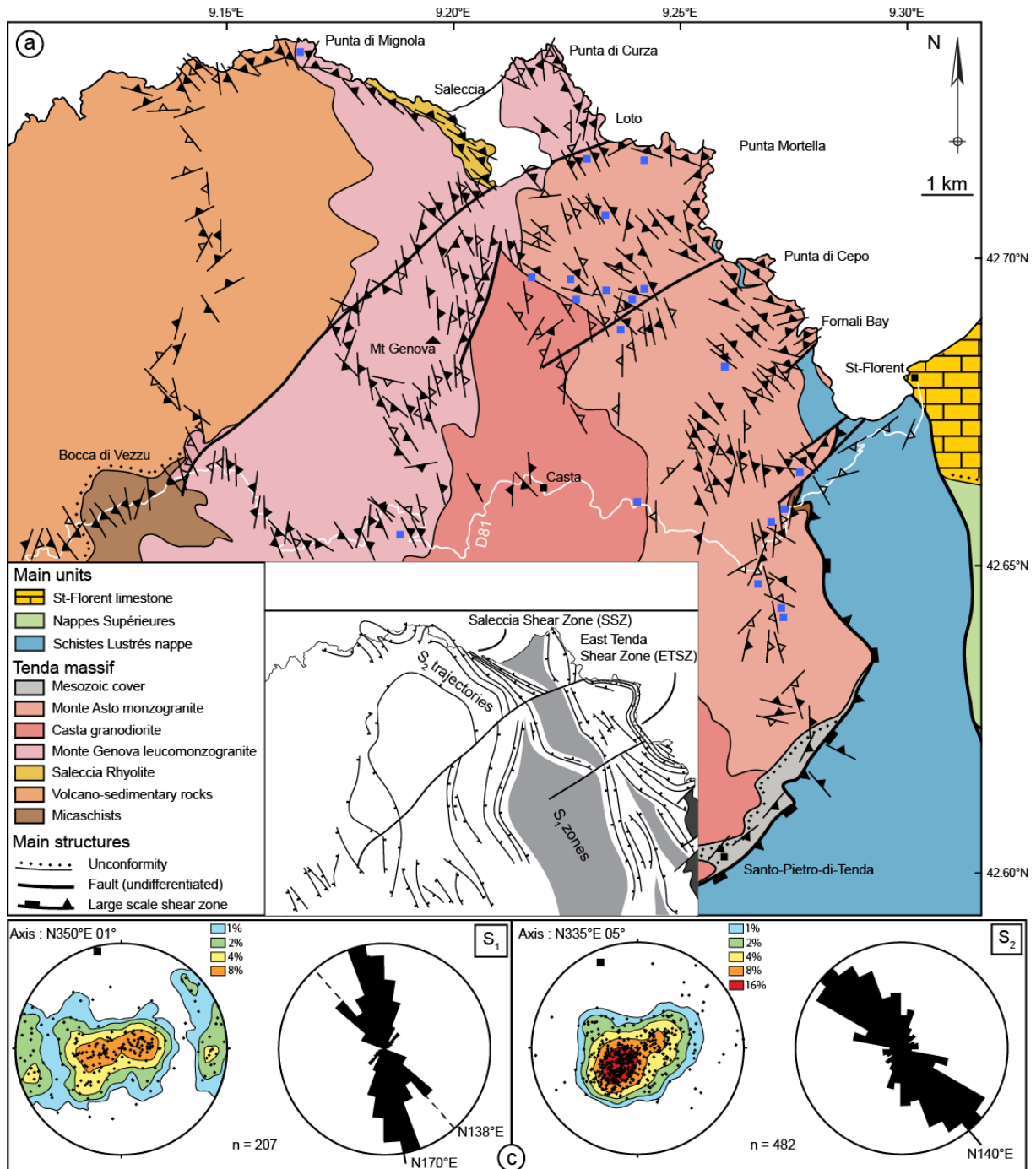


1376

1377

1378 Figure 1

1379

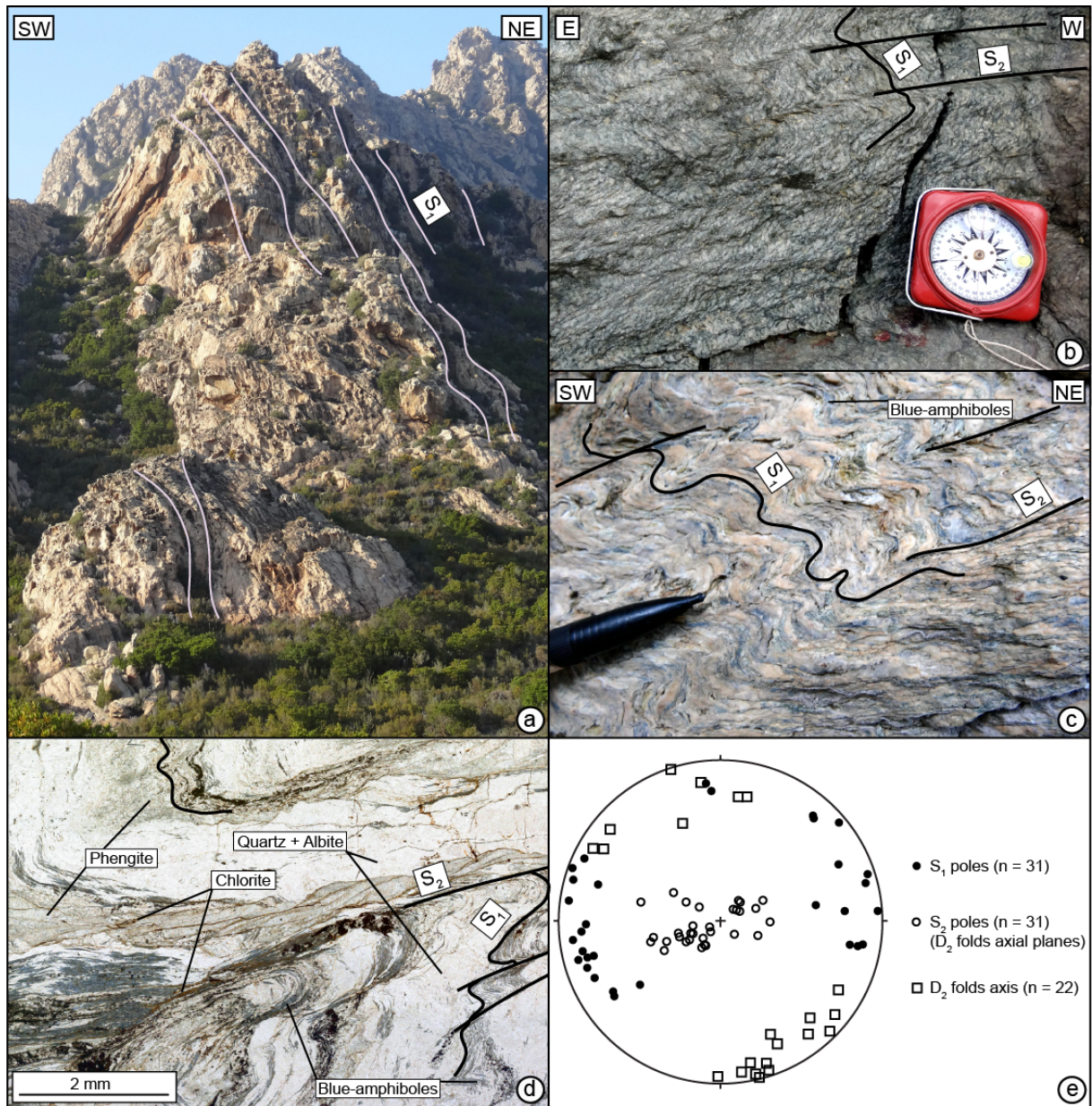


1380

1381

1382 Figure 2

1383

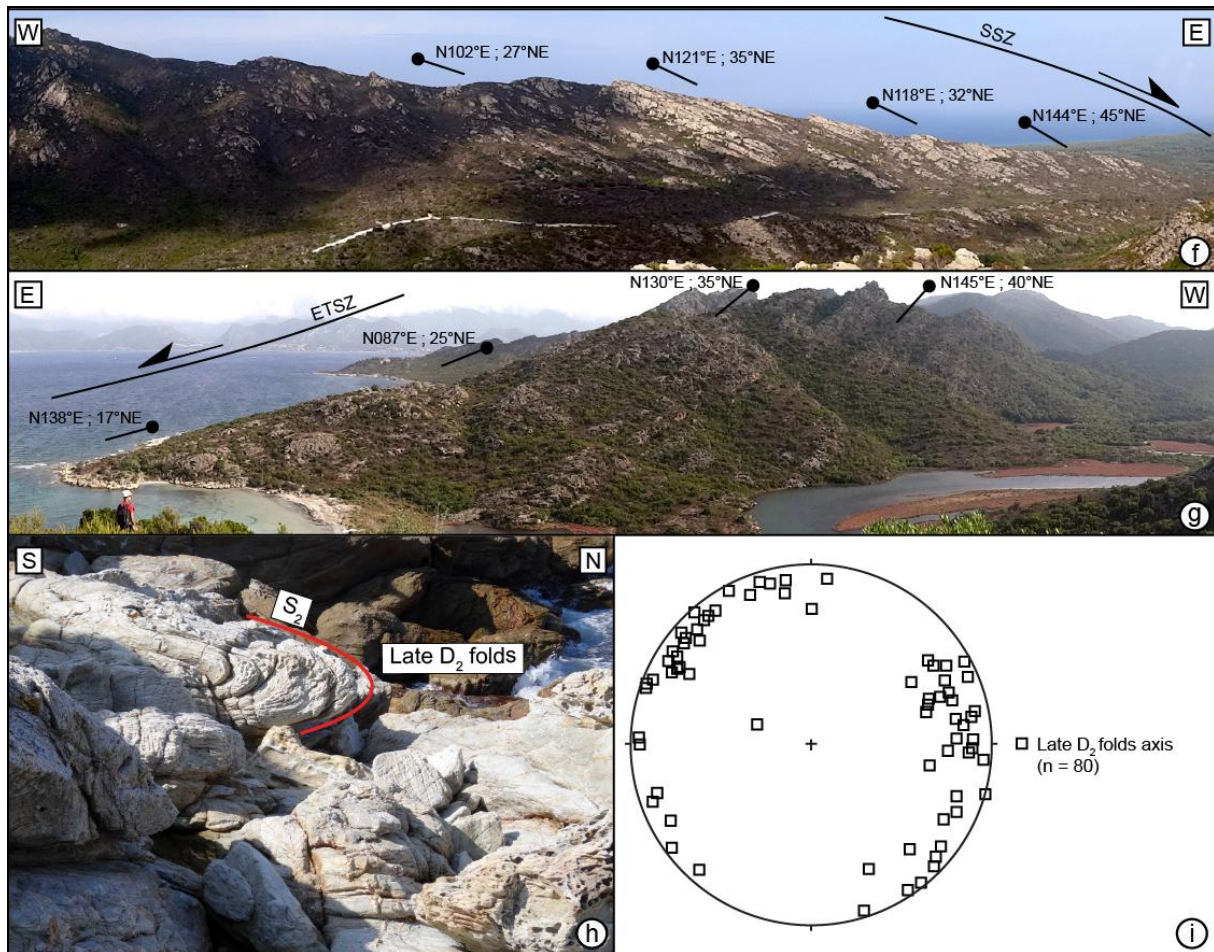


1384

1385

1386 Figure 3-1

1387



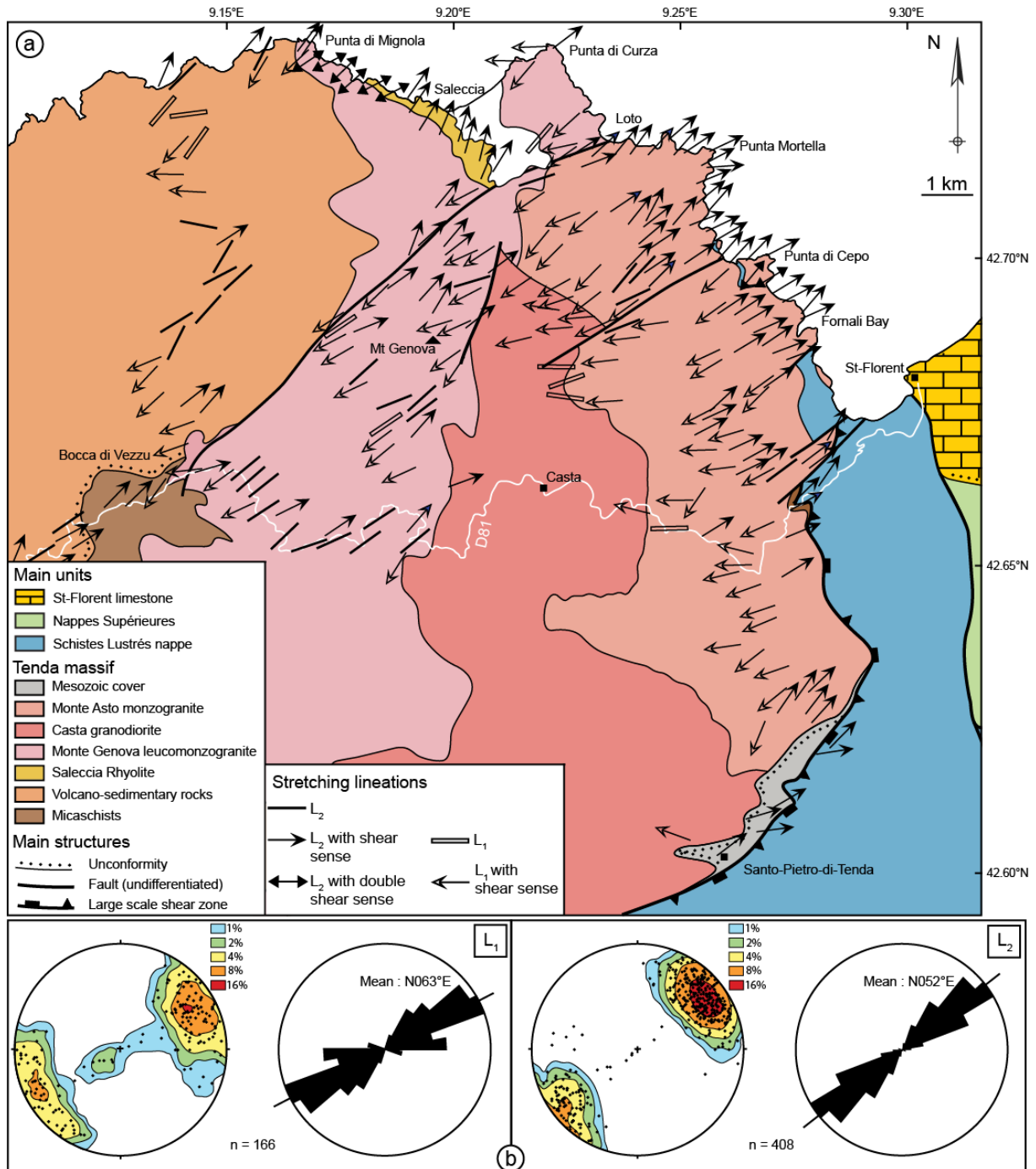
1388

1389

1390 Figure 3-2

1391

1392

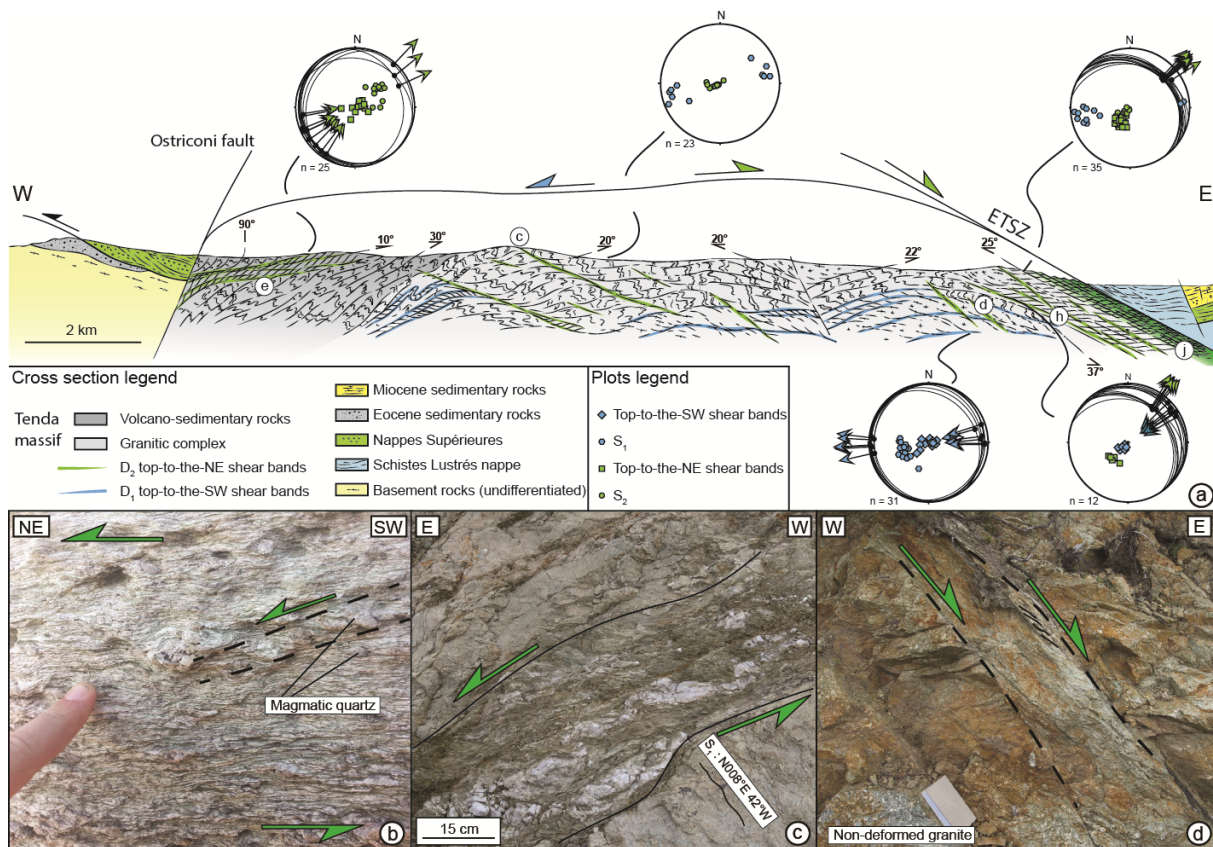


1393

1394

1395 Figure 4

1396

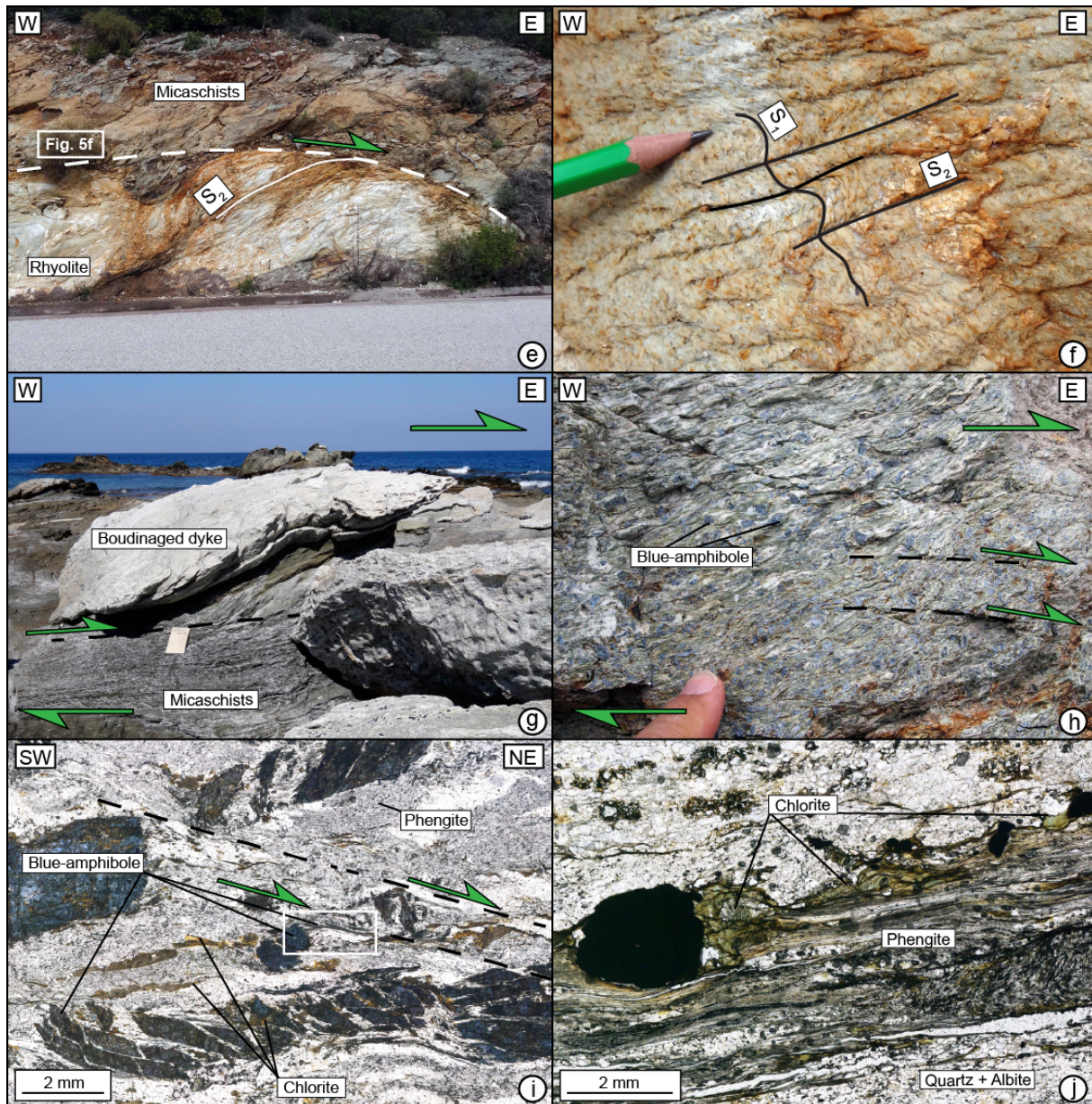


1397

1398

1399 Figure 5-1

1400

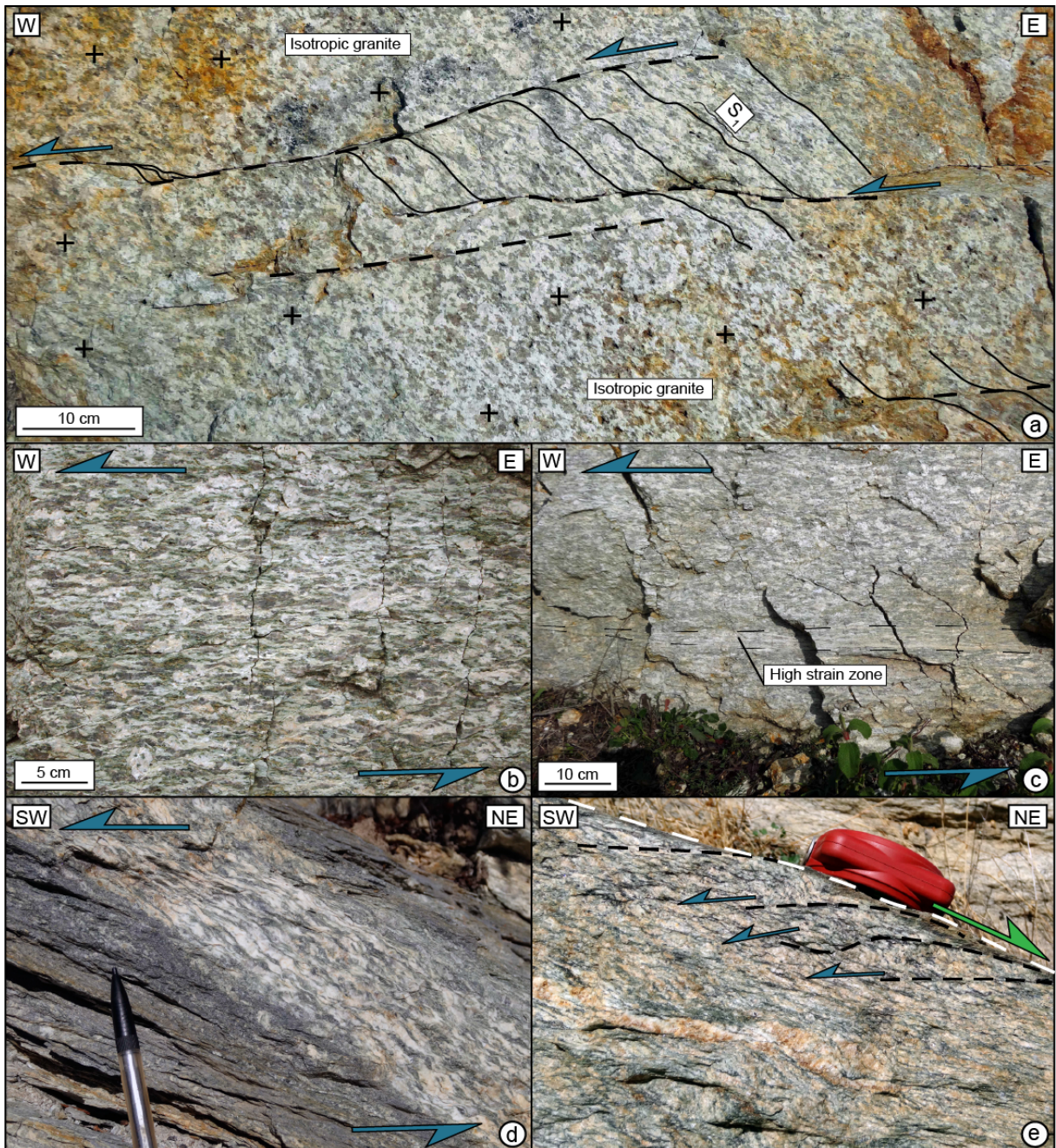


1401

1402

1403 Figure 5-2

1404

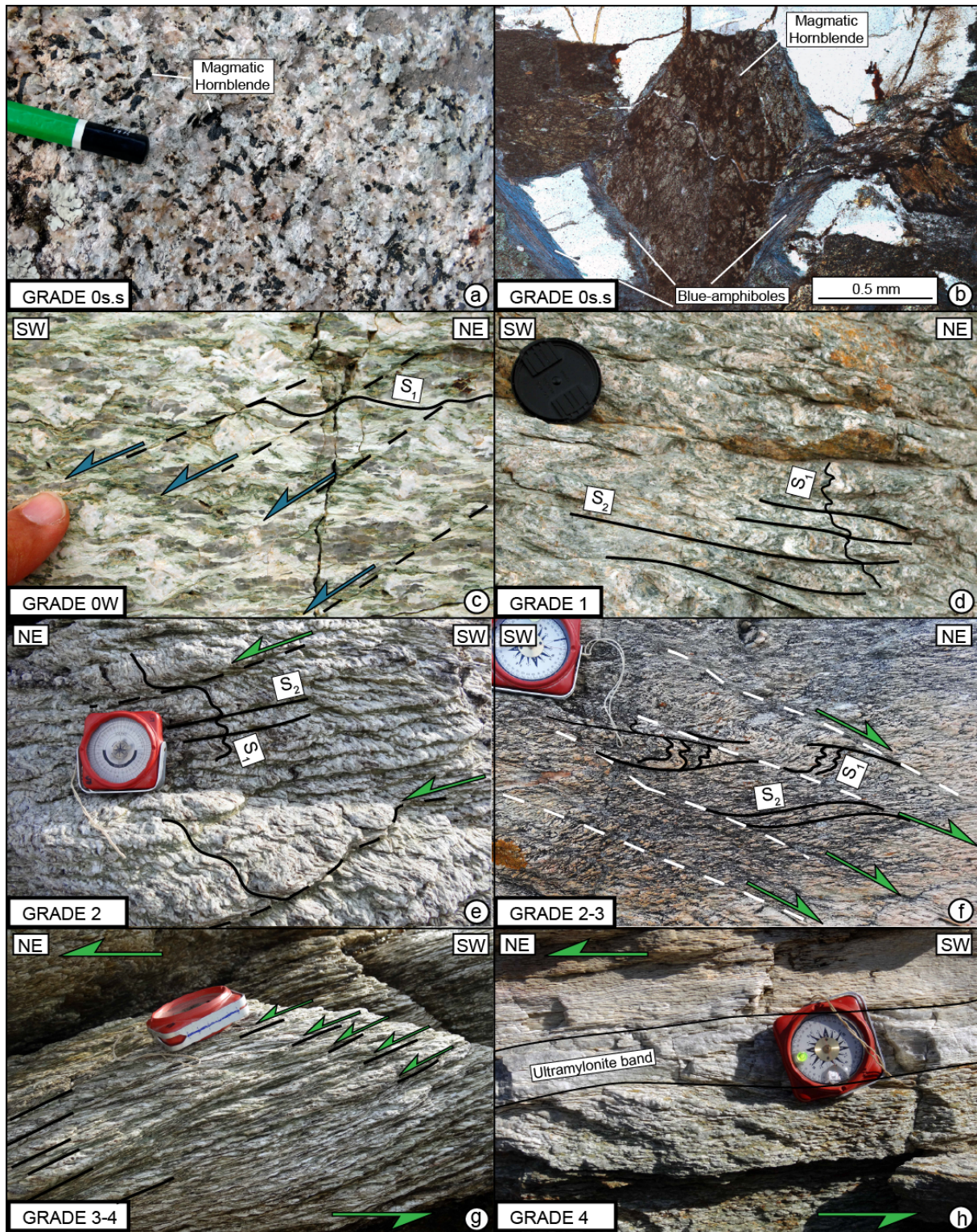


1405

1406

1407 Figure 6

1408

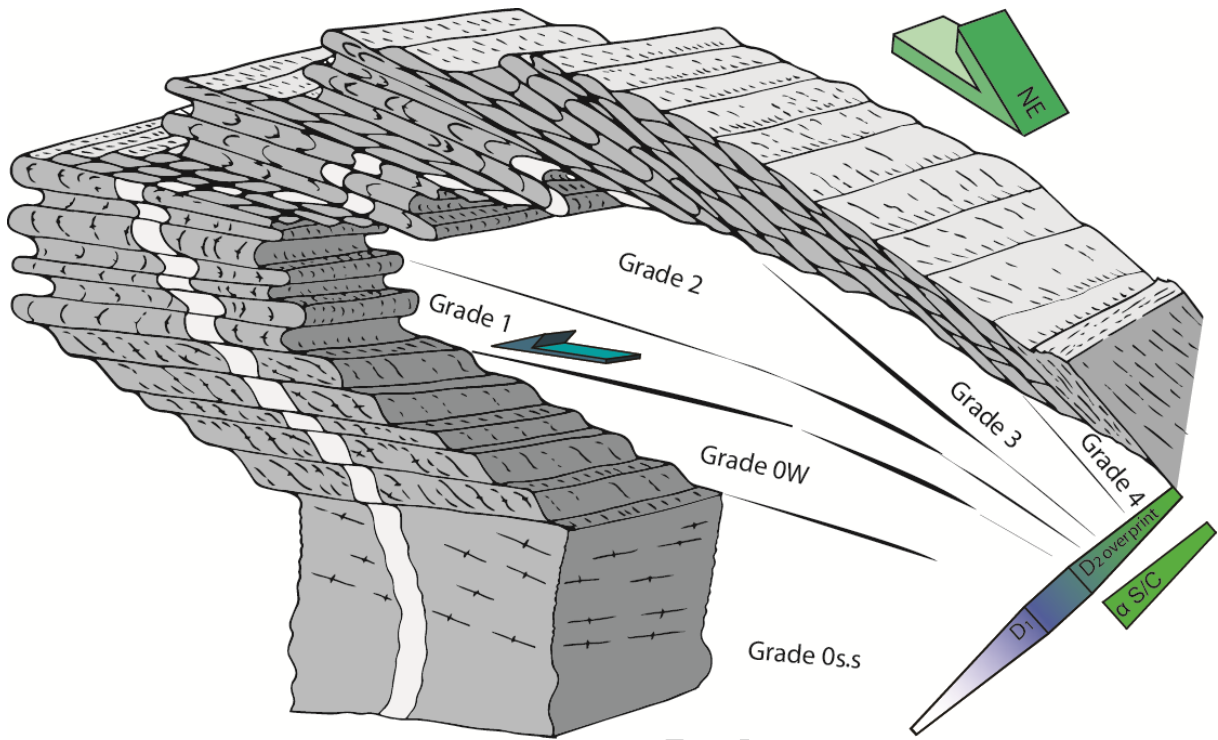


1409

1410

1411 Figure 7

1412

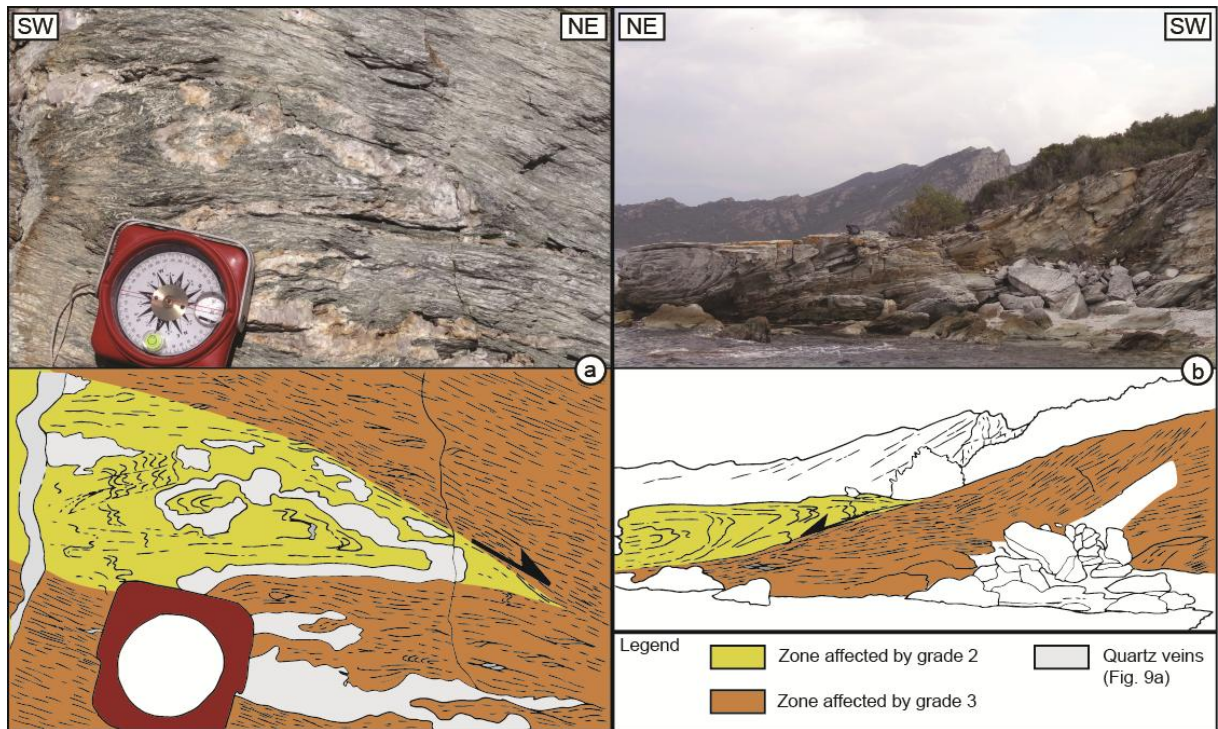


1413

1414

1415 Figure 8

1416

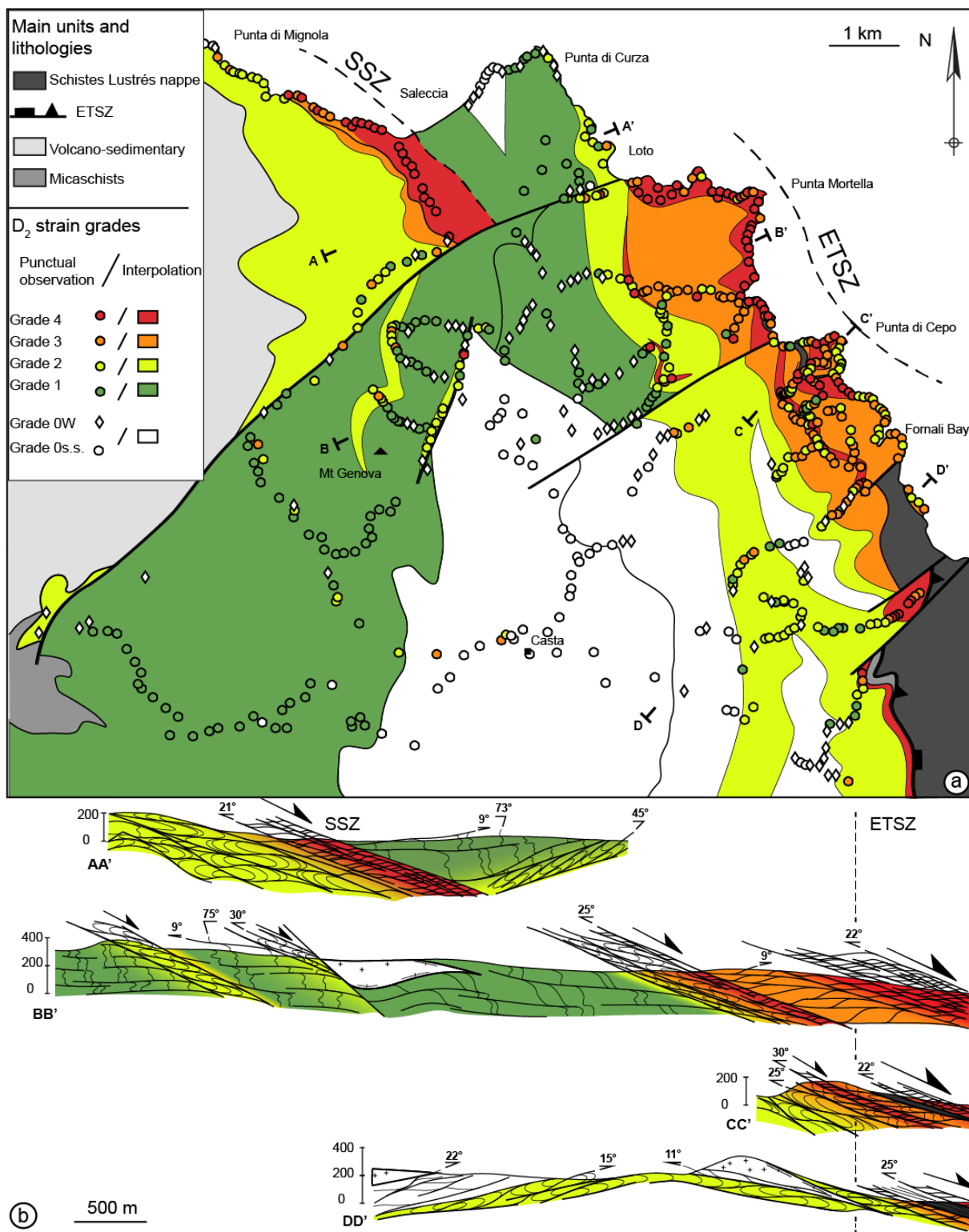


1417

1418

1419 Figure 9

1420

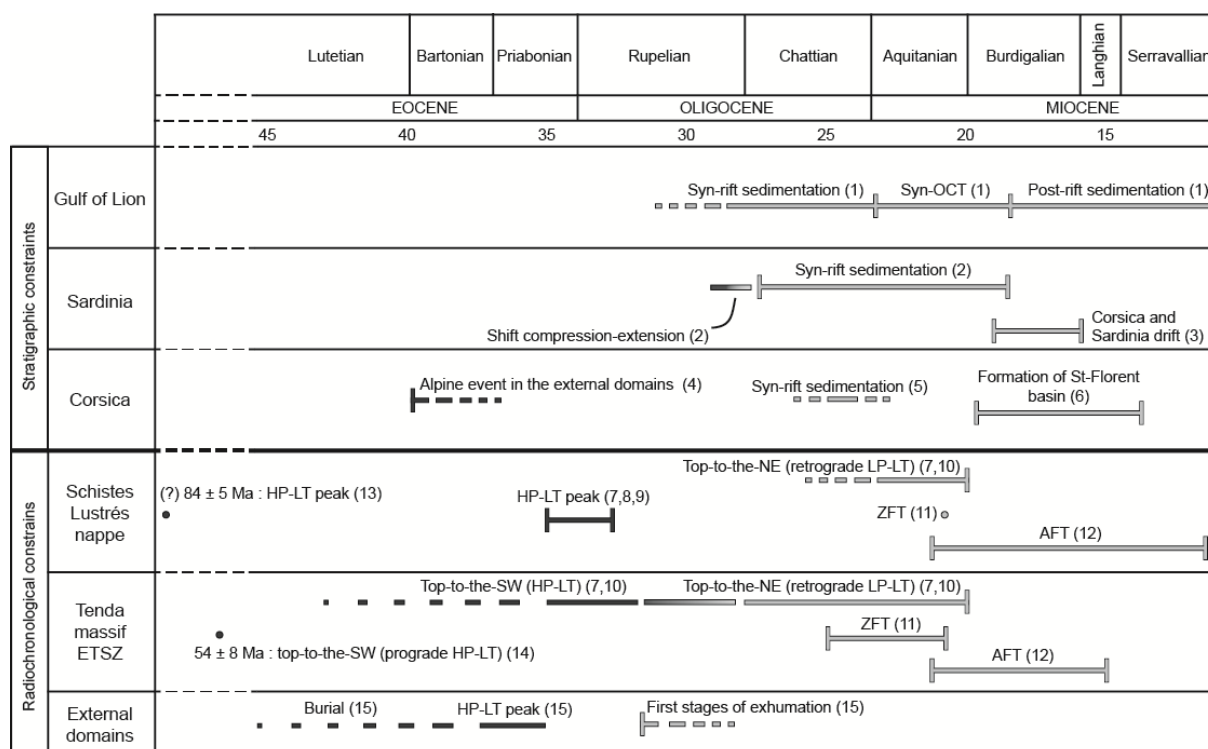


1421

1422

1423 Figure 10

1424

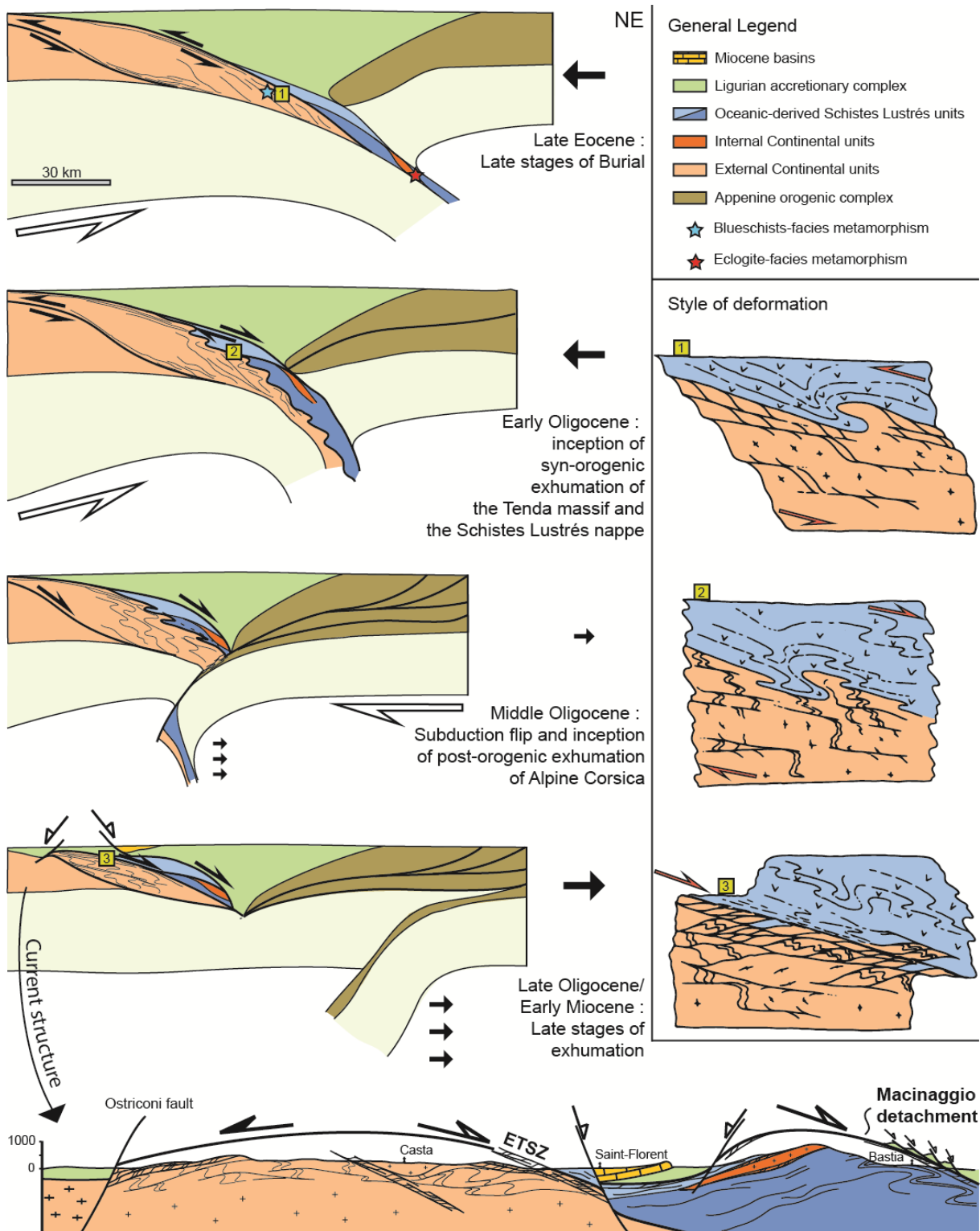


1425

1426

1427 Figure 11

1428



1429

1430

1431 Figure 12

1432

1433 Highlights

1434 The Tenda massif was not rigid, as deformation was pervasive when exhumation started.

1435 Strain mapping shows a strain localization toward the roof and internal shear zones.

1436 The large-scale finite architecture is a dome of extensional-related structures.

1437 Lithological contacts drive strain localization.

1438 Style of deformation was controlled by protolith nature and P-T-fluids conditions.

ACCEPTED MANUSCRIPT